



## O-vacancy-rich porous MnO<sub>2</sub> nanosheets as highly efficient catalysts for propane catalytic oxidation

Shipeng Wu, Huimin Liu, Zhen Huang\*, Hualong Xu, Wei Shen\*

Department of Chemistry, Shanghai Key Laboratory of Molecular Catalysis and Innovative Materials, Laboratory of Advanced Materials, Collaborative Innovation Center of Chemistry for Energy Materials, Fudan University, 220 Handan Road, 200433 Shanghai, China

### ARTICLE INFO

**Keywords:**  
Catalytic oxidation  
Manganese oxide  
Oxygen vacancy  
Propane  
Redox property

### ABSTRACT

Constructing non-noble robust catalysts for deep catalytic oxidation of obstinate light alkanes at low temperature is of great value and significance. Herein, we designed a facile solvent-thermal-reduction strategy to fabricate an O-vacancy-rich porous MnO<sub>2</sub> nanosheet (MnO<sub>2</sub>-PS) catalyst for propane catalytic oxidation. The abundant vacancies in MnO<sub>2</sub>-PS catalysts can significantly promote its redox ability and oxygen activation capacity, and then provide more active oxygen species with enhanced oxygen mobility and reactivity, thus accelerate the cleavage of C-H bond and the decomposition of intermediates. Meanwhile, benefiting from the porous nanosheet structure, MnO<sub>2</sub>-PS catalyst possesses highly accessible surface and high density of exposed active sites, thus facilitating the adsorption and the activation of reactant molecule. At the same time, the catalyst also exhibits good thermal stability and water resistant ability. This robust and efficient catalytic system may provide some enlightenments for designing feasible catalyst with high-performance for deep catalytic destruction of VOCs.

### 1. Introduction

With the rapid development of industrialization and urbanization, air pollution has become one of the most concerned problems in the whole world. The direct emission of volatile organic compounds (VOCs) into the atmosphere will not only pollute the environment, but also, more importantly, endanger the human health [1–4]. Therefore, it is of great significance to develop efficient approaches to control VOCs emission. Compared with the conventional thermal combustion or other control technologies for VOCs abatement, catalytic oxidation is widely regarded as one of the most promising approaches owing to its low ignition temperature, low energy cost, high efficiency, and the clean products (CO<sub>2</sub> and H<sub>2</sub>O) [5–9]. However, the emitted VOCs are diverse and complex in structure. Thereinto, deep catalytic oxidation of saturated alkanes is rather challenging due to the relatively stable molecular structure containing strong C-H bonds. Propane, a representative alkane mainly emitted from petroleum refineries, various industrial processes as well as automobile exhaust, is commonly employed as a model molecule for evaluation of catalyst performance. Supported noble-metal such as Pt and Pd catalysts are effective catalysts for deep catalytic oxidation of propane [10–14]. However, the high cost, poor thermal stability and susceptible to poisoning significantly limit their industrial

applications. Transition metal oxides have been attracted much attention due to their low cost, high thermal stability, resistance to toxicity, and comparable catalytic oxidation activities [15–18].

Manganese oxide, as a typical transition metal oxide, has been widely investigated and applied in versatile oxidation reaction, which attributes to the variable valence states of Mn cations and cost-efficiency as well [19–21]. It is widely accepted that oxygen vacancies (V<sub>O</sub>) in manganese oxide can enable the oxygen involved redox reactions and improve the catalytic activity due to the reversible redox cycle between Mn<sup>4+</sup> and Mn<sup>3+</sup> cations [19,22–25]. However, the activity of manganese oxide used in the deep catalytic oxidation of propane is still insufficient. In order to improve its catalytic performance, researchers have made some attempts. Puertolas et al. [26] reported manganese oxide catalysts prepared by a wet combustion procedure with reductive organic acids as templates for propane deep catalytic oxidation, which exhibited a remarkably higher catalytic activity ( $T_{90} = 265$  °C) than catalyst prepared without the addition of organic acids ( $T_{90} = 310$  °C). The manganese oxide catalysts prepared using glyoxylic acid (Mn-G-350) showed the highest activity was mainly attributed to the highest oxygen mobility and the best redox properties. Lin et al. [27] developed MnO<sub>x</sub> catalysts for propane deep catalytic oxidation by bamboo powder (BP)-mediated biosynthesis with post-treatment of alkaline/acid

\* Corresponding authors.

E-mail addresses: [huangzhen@fudan.edu.cn](mailto:huangzhen@fudan.edu.cn) (Z. Huang), [wshen@fudan.edu.cn](mailto:wshen@fudan.edu.cn) (W. Shen).



washing, resulting the formation of large number of oxygen vacancies and the promotion of reducibility and lattice oxygen mobility. Interestingly,  $\text{MnO}_x\text{-BP-13-1}$  exhibited a much higher reaction rate of  $2.96 \mu\text{mol}\cdot\text{g}_{\text{cat}}^{-1}\cdot\text{s}^{-1}$ , compared with that of  $0.38 \mu\text{mol}\cdot\text{g}_{\text{cat}}^{-1}\cdot\text{s}^{-1}$  on reference  $\text{MnO}_x$  catalyst without BP modification under the same conditions. Jian et al. [28] synthesized four  $\text{MnO}_2$  catalysts with different morphologies and evaluated their performance in the deep catalytic oxidation of propane. The birnessite-type short rod-like  $\text{MnO}_2$  ( $\text{MnO}_2\text{-SR}$ ) exhibits abundant oxygen vacancies, superior reducibility and high surface oxygen mobility, which are responsible for its remarkable activity. They recently prepared three kinds of  $\alpha\text{-MnO}_2$  nanowires supported Au catalysts for oxidation of propane, which exposed (310), (100), and (110) crystal planes, respectively. It shows that  $\alpha\text{-MnO}_2\text{-110}$  with mainly exposed (110) facets possesses largest quantity of oxygen vacancies, strong reducibility, high surface oxygen mobility and with a higher amount of  $\text{Au}^{\delta+}$  species leading to a high ability to adsorb and activate oxygen and propane [29]. Obviously,  $\text{MnO}_x$  materials with unique surface properties, that is, abundant oxygen vacancies and strong redox ability and oxygen mobility, would be promising catalysts for propane deep catalytic oxidation. However, the reported catalyst systems still have some obvious shortcomings to be improved, such as insufficient low-temperature activity, complicated morphology and/or crystal plane controlled operation. Furthermore, in the real exhaust condition, water is often contained and it itself is also one of the products of VOCs deep catalytic oxidation. Therefore, to evaluate the activity of the catalyst under simulating the real exhaust emissions conditions is more needed and meaningful. Moreover, a deep understanding of promotional effects of oxygen vacancies and the reaction mechanism over the manganese catalysis remains elusive.

Herein, in this work we successfully synthesized porous  $\text{MnO}_2$  nanosheets catalysts with abundant oxygen vacancies via a solvent-thermal reaction method. The catalysts exhibited excellent catalytic activity and stability in propane catalytic oxidation. The textural property, oxygen vacancy and redox behavior, which the key factors affecting the catalytic performance were investigated. The corresponding structure–activity relationship and reaction mechanism were elucidated.

## 2. Experimental

### 2.1. Materials and reagents

All the chemicals were commercial products and used directly. Polyvinylpyrrolidone (PVP, 98%, M.W. = 1300,000),  $\text{MnSO}_4\cdot\text{H}_2\text{O}$  (AR), Mn ( $\text{CH}_3\text{COO}$ )<sub>2</sub>·4 H<sub>2</sub>O (AR), and  $\text{KMnO}_4$  (AR) were provided by Acros Organics. Urea (AR) and ethylene glycol (99%) were purchased from Sinopharm Chemical Reagent Co. Ltd (China).

### 2.2. Preparation of catalyst

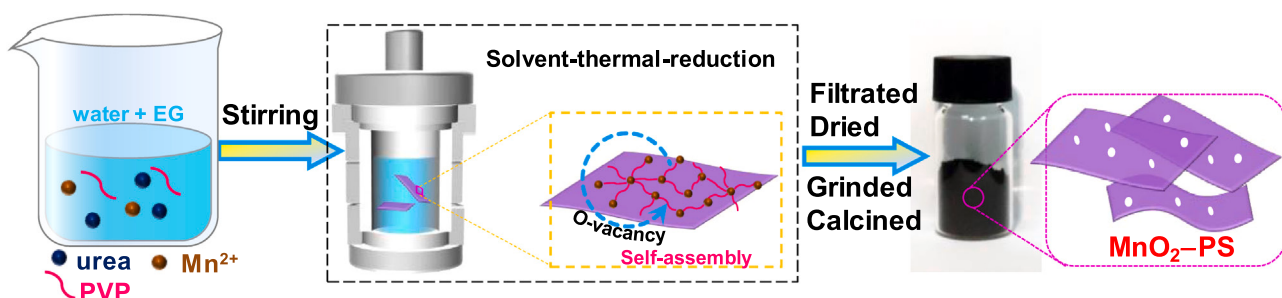
The porous  $\text{MnO}_2$  nanosheets (denoted as  $\text{MnO}_2\text{-PS}$ ) with abundant oxygen vacancies were prepared by a modified solvent-thermal-

reduction strategy [6] and the synthetic process was illustrated in Scheme 1. Typically, 0.3 g of PVP was dissolved in a mixed solution of 60 mL distilled water and 60 mL ethylene glycol, then, 2.45 g of Mn ( $\text{CH}_3\text{COO}$ )<sub>2</sub>·4 H<sub>2</sub>O was added under continuous stirring at room temperature for 0.5 h. Subsequently, 3.0 g of urea was added and stirred for another 0.5 h. Afterwards, the above solution was poured into a 200 mL Teflon-lined stainless-steel autoclave and maintained at 180 °C for 6 h. The obtained products were collected by filtration and washed with deionized water and ethanol several times. Finally, the solids were dried in oven at 120 °C for 12 h and calcined at 400 °C (2 °C min<sup>-1</sup>) for 4 h in air.

For comparison, a rod-like  $\text{MnO}_2$  (denoted as  $\text{MnO}_2\text{-R}$ ) which was reported decent catalytic performance for propane oxidation as well as other VOCs [24,28,30–32] and a typical bulk  $\text{MnO}_2$  catalyst (denoted as  $\text{MnO}_2\text{-B}$ , purchased from Alfa Aesar and pretreated at 400 °C for 4 h in air) were also studied as the reference samples. The  $\text{MnO}_2\text{-R}$  was prepared by the following reported hydrothermal redox method [31]. Typically, 1.0 g of  $\text{MnSO}_4\cdot\text{H}_2\text{O}$  and 2.4 g of  $\text{KMnO}_4$  were mixed in 120 mL of distilled water under stirring at 600 rpm for 0.5 h at room temperature. Then, this mixture solution was transferred into a 200 mL Teflon-lined stainless-steel autoclave and heated at 140 °C for 12 h. The resulting products were filtered and washed with deionized water and ethanol several times. Finally, the solids were dried in oven at 120 °C overnight and calcined in air at 400 °C (2 °C min<sup>-1</sup>) for 4 h.

### 2.3. Characterizations of catalyst

The X-ray diffraction (XRD) analysis were performed in a Bruker D8 Advance A25 diffractometer with  $\text{CuK}\alpha$  radiation ( $\lambda = 0.154 \text{ nm}$ ) and the XRD patterns were recorded in the range of 10°–80° (2θ) with a measured rate of 0.02° per 0.2 s. The  $\text{N}_2$  adsorption-desorption isotherms were obtained at 77 K on an automated analyser (Micromeritics TriStar II 3020). Before measurements, the samples were previously degassed at 300 °C for 8 h. The specific surface areas and pore size distribution were calculated based on BET and BJH methods, respectively. High transmission electron microscopy (HRTEM) images of samples were recorded on a FEI Tecnai G2 F20 S-Twin microscope with an acceleration voltage of 200 kV. X-ray photoelectron spectroscopy (XPS) analysis were performed on an RBD upgraded PHI-5000 C ESCA system and the binding energy shift due to the surface charging was adjusted based on the C 1 s line at 284.5 eV. The hydrogen temperature-programmed reduction ( $\text{H}_2\text{-TPR}$ ) and oxygen temperature-programmed desorption ( $\text{O}_2\text{-TPD}$ ) was tested on a Micromeritics AutoChem II 2920 chemisorption analyzer and the sample was calcined at 300 °C for 2 h under  $\text{O}_2$  atmosphere before each test. For  $\text{H}_2\text{-TPR}$ , 100 mg of catalyst was pretreated with 10 vol%  $\text{H}_2$ -90 vol% He mixed gas flow (30 mL min<sup>-1</sup>) at 50 °C for 0.5 h, after which the data was collected in a temperature range of 50–800 °C at a rate of 10 °C min<sup>-1</sup>. For  $\text{O}_2\text{-TPD}$ , 100 mg of catalyst was first treated under He flow (30 mL min<sup>-1</sup>) at 200 °C for 0.5 h. After cooled down to 50 °C, the sample was exposed to a 5 vol%  $\text{O}_2$ -95 vol% He mixed gas flow (30 mL min<sup>-1</sup>) for 1 h. Then, He (30 mL min<sup>-1</sup>) was switched in order to purge the gas-phase  $\text{O}_2$  from



Scheme 1. Synthetic strategy for  $\text{MnO}_2\text{-PS}$  catalyst.

the sample until the baseline was stable. Finally, the sample was raised to 800 °C at a rate of 10 °C min<sup>-1</sup> under He flow. Low-temperature electron paramagnetic resonance (EPR) spectra were obtained on a Bruker A300 at 100 K at X-band frequencies (9.4 GHz) by using a 100-kHz field modulation frequency and a 1.0-G standard modulation amplitude. The spin concentration was calculated based on the DPPH standard.

*In situ* diffuse reflectance infrared Fourier transform spectroscopy (*in situ* DRIFTS) were collected on a Nicolet 6700 spectrometer. All DRIFT spectra were gathered in the Kubelka-Munk format, accumulating 64 scans per minute at 4 cm<sup>-1</sup> resolution. Prior to each test (catalyst filling amount: 25 mg), the sample was pre-treated at 300 °C under He flow for 1 h to remove the surface impurities. After the background spectrum was collected at 200 °C, the catalysts were exposed to a flow of 5 vol% C<sub>3</sub>H<sub>8</sub> – 95 vol% N<sub>2</sub> and *in situ* DRIFTS spectra of the catalyst were recorded as a function of time until adsorption equilibrium. After that, *In-situ* DRIFTS spectra of propane oxidation (0.2 vol% C<sub>3</sub>H<sub>8</sub>, 2.4 vol% O<sub>2</sub>/N<sub>2</sub>) of the catalyst (catalyst filling amount: 25 mg) were recorded as a function of temperature at 50–300 °C.

All density functional theory (DFT) with spin polarization calculations were performed by the Vienna Ab Initio Simulation Package (VASP) code. The Perdew-Burke-Ernzerhof (PBE) functional within the generalized gradient approximation (GGA) was adopted to describe electronic exchange-correlation energy. The ionic cores were described with the projector augmented wave (PAW) method. And in the z-directions, the structure was separated by 15 Å vacuum height from its neighbors. A basis set of plane waves was up to an energy cutoff of 450 eV. The localized d electrons correlation for Mn metal can be described by DFT+U method. For the structure optimization and energy calculations, the K-points of the MnO<sub>2</sub>–PS (100), MnO<sub>2</sub>–R (200), MnO<sub>2</sub>–B (110) slab models were set to be 3 × 2 × 1, 3 × 3 × 1, 3 × 2 × 1, respectively. All of the calculations were continued until the force and energy have converged to less than 0.02 eV Å<sup>-1</sup> and 10<sup>-5</sup> eV Å<sup>-1</sup>, respectively.

The adsorption energies (E<sub>ads</sub>) of the C<sub>3</sub>H<sub>8</sub> was calculated using the following equation:

$$E_{\text{ads}} = E_{\text{complex}} - E_{\text{surface}} - E_{\text{gas}}$$

Where E<sub>complex</sub> represents the energy of MnO<sub>2</sub> after C<sub>3</sub>H<sub>8</sub> adsorption, E<sub>surface</sub> is the energy of MnO<sub>2</sub> and E<sub>gas</sub> is the energy of isolated C<sub>3</sub>H<sub>8</sub>, respectively.

#### 2.4. Catalytic activity measurement

All evaluation experiments of the catalysts for C<sub>3</sub>H<sub>8</sub> catalytic oxidation were measured in a continuous flow fixed-bed reactor. A total of 100 mg of catalyst (40–60 mesh) was diluted with 300 mg quartz sand of the same size in order to eliminate internal and external diffusion. The total flow rate of the inlet gas (5 vol% H<sub>2</sub>O, 0.2 vol% C<sub>3</sub>H<sub>8</sub>, 2 vol% O<sub>2</sub>, and N<sub>2</sub> balance) was kept at 50 mL min<sup>-1</sup>, (weight hourly space velocity: WHSV = 30,000 mL·g<sup>-1</sup>·h<sup>-1</sup>). The conversion of C<sub>3</sub>H<sub>8</sub> and the yield of CO<sub>2</sub> were measured by a GC-7900 online gas chromatography (Techcomp, China) equipped with a hydrogen flame ionization detector (FID) and a thermal conductivity detector (TCD), respectively.

The conversion of C<sub>3</sub>H<sub>8</sub> and the yield of CO<sub>2</sub> were calculated as follows:

$$\text{Conversion(C}_3\text{H}_8\text{)} = \frac{[\text{C}_3\text{H}_8]_{\text{in}} - [\text{C}_3\text{H}_8]_{\text{out}}}{[\text{C}_3\text{H}_8]_{\text{in}}} \times 100\%$$

$$\text{Yield(CO}_2\text{)} = \frac{[\text{CO}_2]_{\text{out}}}{3 \times [\text{C}_3\text{H}_8]_{\text{in}}} \times 100\%$$

where [C<sub>3</sub>H<sub>8</sub>]<sub>in</sub>, [C<sub>3</sub>H<sub>8</sub>]<sub>out</sub> and [CO<sub>2</sub>]<sub>out</sub> represent the inlet C<sub>3</sub>H<sub>8</sub> concentration, the outlet C<sub>3</sub>H<sub>8</sub> concentration and the outlet CO<sub>2</sub> concentration, respectively.

The reaction rate (r, μmol g<sup>-1</sup> s<sup>-1</sup>) was calculated as follows:

$$r = \frac{10^3 \times V \cdot C \cdot X_{\text{C}_3\text{H}_8}}{3600 \times R}$$

where V represents the weight hourly space velocity (mL·g<sup>-1</sup>·h<sup>-1</sup>), C is the concentration of feeding C<sub>3</sub>H<sub>8</sub>, X<sub>C3H8</sub> is the conversion of C<sub>3</sub>H<sub>8</sub>, R is the standard molar volume of gas (22.4 L/mol).

The intrinsic turnover frequency (iTOF, h<sup>-1</sup>) of the catalysts, defined as the moles of propane converted at the initial state per mole of surface Mn atoms or chemisorbed oxygen species per unit time [19].

$$\text{iTOF(h}^{-1}\text{)} = \frac{\text{initial conversion rate}}{n}$$

where n represents the surface/sub-surface Mn atoms or chemisorbed oxygen species (mmol g<sup>-1</sup>), the calculation details were described in supplementary information.

The specific activity and apparent activation energy were also calculated.

### 3. Results and discussion

#### 3.1. Comprehensive characterization of catalysts

##### 3.1.1. Structures and morphology

The XRD patterns of the MnO<sub>2</sub>–PS, MnO<sub>2</sub>–R and MnO<sub>2</sub>–B catalysts are shown in Fig. 1A. The MnO<sub>2</sub>–PS displays a hexagonal phase of ε-MnO<sub>2</sub> (a = 2.8000 Å and c = 4.4500 Å, JCPDS#30-0820). In addition, it was found that the precursor of MnO<sub>2</sub>–PS is mainly in the crystal structure of MnCO<sub>3</sub> phase before calcination (Fig. S1). For the pattern of MnO<sub>2</sub>–R, all diffraction peaks can be attributed to a tetragonal phase of α-MnO<sub>2</sub> (a = 9.7847 Å and c = 2.8630 Å, JCPDS#44-0141). As compared, MnO<sub>2</sub>–B shows much sharper and stronger diffraction peaks, which are matched well with characteristic diffraction of orthorhombic phase of β-MnO<sub>2</sub> (a = 4.4370 Å, b = 4.3120 Å and c = 2.8620 Å, JCPDS#50-0866). However, the peak intensity of MnO<sub>2</sub>–PS catalyst is relatively low, which would probably due to large number of defect sites in MnO<sub>2</sub>–PS catalyst, leading to a decrease in crystallinity. Moreover, the average crystal size of samples was calculated in Table 1. The mean crystal size of MnO<sub>2</sub>–PS was about 10.5 nm, which is much smaller than that of prepared MnO<sub>2</sub>–R catalyst (24.4 nm) and commercial MnO<sub>2</sub>–B catalyst (46.6 nm).

As shown in Fig. 1B, all of the catalysts display unique type IV isotherms with an obvious H3-type hysteresis loop [29,31]. Combined with the pore size distribution, as shown in Fig. 1C and Table 1, which evidences the existence of a mesoporous structure with different particle packing types of these MnO<sub>2</sub> catalysts [28,31]. Notably, compared with MnO<sub>2</sub>–R and MnO<sub>2</sub>–B catalysts, the MnO<sub>2</sub>–PS catalyst exhibits a more obvious pore property and possesses mesoporous with main pore size of ca. 8 nm (Fig. 1C). As summarized in Table 1, the BET specific surface area (S<sub>BET</sub>) and the pore volume (V<sub>p</sub>) of the MnO<sub>2</sub>–PS catalyst are 74 m<sup>2</sup> g<sup>-1</sup> and 0.22 cm<sup>3</sup> g<sup>-1</sup>, respectively, which are obviously higher than those of MnO<sub>2</sub>–R catalyst (34 m<sup>2</sup> g<sup>-1</sup> and 0.18 cm<sup>3</sup> g<sup>-1</sup>) and MnO<sub>2</sub>–B catalyst (13 m<sup>2</sup> g<sup>-1</sup> and 0.01 cm<sup>3</sup> g<sup>-1</sup>). This phenomenon may be explained by its smaller grain size of MnO<sub>2</sub>–PS catalyst, which is agreement with XRD results. As thus, it would probably provide more active sites and effective substrate transportation, leading to the enhanced catalytic activity of the catalysts [33,34]. The micromorphology of MnO<sub>2</sub>–PS, MnO<sub>2</sub>–R and MnO<sub>2</sub>–B were investigated by TEM, as shown in Fig. 2. The MnO<sub>2</sub>–PS exhibited a nano-sheet structure with many holes and rough surface, and the average edge length and thickness of MnO<sub>2</sub>–PS are ca. 50–100 and 10–15 nm, respectively (Figs. 2A and S2). The MnO<sub>2</sub>–R displayed a non-uniform rod-like morphology with a diameter of about 30 nm and 200–400 nm in length (Fig. 2B). The morphology of MnO<sub>2</sub>–B showed a commonly irregular bulk structure (Fig. 2C). Furthermore, the HRTEM images corresponding

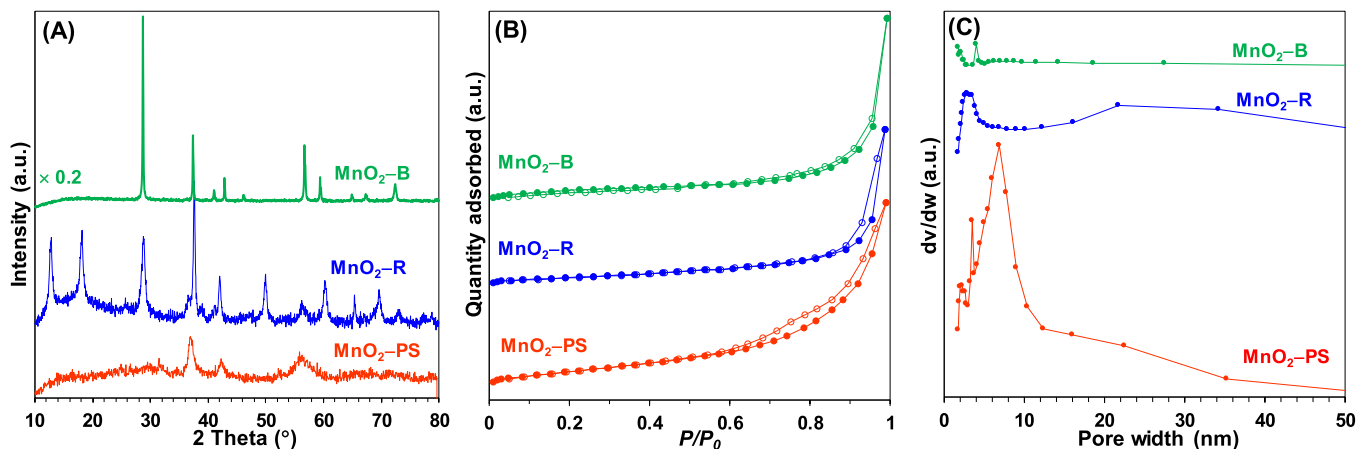


**Fig. 1.** (A) XRD patterns, (B)  $N_2$  isotherms and (C) the corresponding pore size distributions of  $MnO_2$ -PS,  $MnO_2$ -R and  $MnO_2$ -B catalysts.

**Table 1**

Crystal size and textural parameters of  $MnO_2$ -PS,  $MnO_2$ -R and  $MnO_2$ -B catalysts.

Catalyst	Crystal size (nm) <sup>a</sup>	$S_{BET}$ ( $m^2 g^{-1}$ )	$V_p$ ( $cm^3 g^{-1}$ ) <sup>b</sup>	$D_p$ (nm) <sup>b</sup>
$MnO_2$ -PS	10.5	74	0.22	10.4
$MnO_2$ -R	25.4	34	0.18	19.5
$MnO_2$ -B	46.6	13	0.01	17.9

<sup>a</sup> Calculated by the Scherrer equation from the (100), (200) and (110) plane of  $MnO_2$ -PS,  $MnO_2$ -R and  $MnO_2$ -B, respectively. <sup>b</sup> Measured by the BJH method.

FFT (insets images) show that the  $MnO_2$ -PS mainly exposes an interplanar spacing of 0.242 nm attributed to the (100) facet, while the  $MnO_2$ -R and  $MnO_2$ -B catalysts show the (200) and (110) lattice plane with interplanar spacing of 0.489 nm and 0.309 nm, respectively (Fig. 2D-F). Compared with  $MnO_2$ -R and  $MnO_2$ -B catalysts, the rough surface and porous structure of  $MnO_2$ -PS nanosheets can contribute to the exposure of active sites and the mass transfer, leading to the enhanced catalytic activity [35,36].

### 3.1.2. Redox properties

The redox properties of these series catalyst were comprehensively

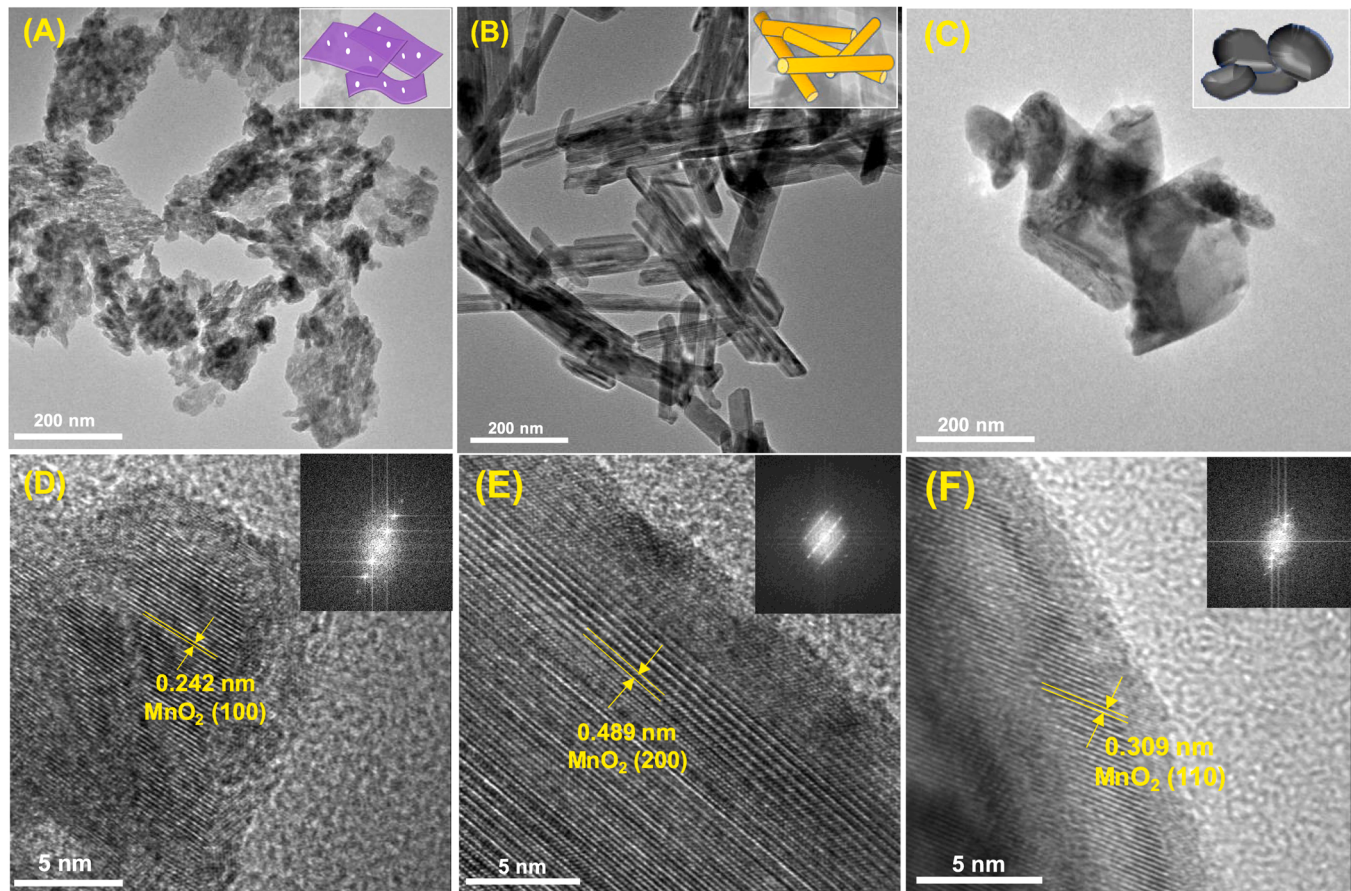


**Fig. 2.** TEM and HR-TEM (insets: FFT images) images of (A, D)  $MnO_2$ -PS, (B, E)  $MnO_2$ -R and (C, F)  $MnO_2$ -B catalysts.

investigated by H<sub>2</sub>-TPR and O<sub>2</sub>-TPD. As shown in Fig. 3A, there are mainly two obvious reduction peaks at ca. 250–400 °C and 400–550 °C for all samples, which can be assigned to the successive reduction of MnO<sub>2</sub> → Mn<sub>3</sub>O<sub>4</sub> → MnO [29,37]. Notably, there are extra small peaks respectively at ca. 201 °C, 232 °C and 248 °C for MnO<sub>2</sub>-PS, MnO<sub>2</sub>-R and MnO<sub>2</sub>-B, which can be attributed to the reduction of surface chemisorbed oxygen species (O<sub>ads</sub>) [19]. In addition, the reduction temperatures related to the reduction of MnO<sub>2</sub> to Mn<sub>3</sub>O<sub>4</sub> and Mn<sub>3</sub>O<sub>4</sub> to MnO for MnO<sub>2</sub>-PS catalyst are 322 °C and 432 °C, respectively, which are both much lower than those of MnO<sub>2</sub>-R catalyst (355 °C and 450 °C) and MnO<sub>2</sub>-B catalyst (386 °C and 513 °C). It may be attributed to the large defects present on the surface of MnO<sub>2</sub>-PS catalysts resulted in the weakening of the Mn–O bond [3,38]. These results clearly reveal a superior reducibility of MnO<sub>2</sub>-PS catalyst. On the other hand, the type of oxygen species in the catalysts were identified by O<sub>2</sub>-TPD. As presented in Fig. 3B, the desorption peak at ca. 450–600 °C can be attributed to the lattice oxygen species in the surface, while the peak at higher temperature (> 600 °C) to the bulk lattice oxygen species [39,40]. In addition, there is a weak shoulder peak at ca. 386 °C for MnO<sub>2</sub>-PS catalyst. It can be ascribed to the defect species (i.e., O<sub>2</sub><sup>−</sup>, O<sup>−</sup>), which are generated at oxygen vacancies on the surface of the MnO<sub>2</sub>-PS catalyst [37,41]. Notably, the MnO<sub>2</sub>-PS catalyst exhibits much lower desorption temperature of lattice oxygen species among the investigated catalysts. These phenomena indicate the presence of abundant oxygen vacancies with enhanced oxygen mobility and oxygen storage capacity of MnO<sub>2</sub>-PS catalyst, which are good agreement with the TPR analysis.

### 3.1.3. Oxygen vacancies and surface properties

As is well recognized, low-temperature EPR spectrum is a powerful technology to verify and measure the oxygen vacancies (V<sub>O</sub>) on the surface of oxides. Thus, an in-depth exploration of oxygen vacancies in the MnO<sub>2</sub>-PS, MnO<sub>2</sub>-R and MnO<sub>2</sub>-B catalysts were carried out. A signal at ca. 3515 G (Fig. 4A) and a free electron factor (*g*) at ca. 2.003 (Fig. 4B), which can be attributed to the typical V<sub>O</sub> in MnO<sub>2</sub> related with the defective oxygen species (i.e., O<sub>2</sub><sup>−</sup> and O<sup>−</sup>) [19,41]. Moreover, the quantitative results further evidence that the MnO<sub>2</sub>-PS has an obviously higher concentration of oxygen vacancies (10.6 × 10<sup>18</sup> spins·g<sup>−1</sup>) than those on MnO<sub>2</sub>-R (ca. 8.1 × 10<sup>18</sup> spins·g<sup>−1</sup>) and MnO<sub>2</sub>-B (ca. 6.1 × 10<sup>18</sup> spins·g<sup>−1</sup>) [19,41].

Following that, the surface features of the series catalysts were further unraveled by XPS. As shown in Fig. 5, deconvolution of the Mn 2p<sub>3/2</sub> region can be resolved into two peaks, and the binding energies

(BEs) at ca. 642.2 eV and 643.4 eV can be ascribed to Mn<sup>3+</sup> and Mn<sup>4+</sup> species, respectively [42,43]. In addition, the O 1 s core level can be well resolved into three peaks. Specifically, the peak at ca. 529.9 eV can be attributed to lattice O species (i.e., O<sup>2−</sup>, donated as O<sub>latt</sub>), while the peak at ca. 531.8 eV can be assigned to the surface-adsorbed reactive O<sub>ads</sub> species (i.e., O<sub>2</sub><sup>−</sup> and O<sup>−</sup>, donated as O<sub>β</sub>), which are closely associated with the active oxygen vacancies (V<sub>O</sub>) [28,44]. Meanwhile, the peak at a higher BE ca. 533.4 eV corresponds to O species of adsorbed OH groups from weakly oxygen and water (i.e., O<sub>OH</sub>, donated as O<sub>γ</sub>) [28,44]. Furthermore, since the binding energies of different Mn valences in Mn 2p spectra are very close, the Mn 3 s XPS deconvolution results were also provided (Fig. S3) and the average oxidation state (AOS) of Mn can be estimated based on the binding energy difference of Mn 3 s [28,34]. As listed in Table 2, the MnO<sub>2</sub>-PS among the series catalysts exhibits the lowest AOS, highest Mn<sup>3+</sup>/Mn<sup>4+</sup> and O<sub>ads</sub>/O<sub>latt</sub> ratio. These results convince that the MnO<sub>2</sub>-PS catalyst possess abundant oxygen vacancies, plentiful active oxygen species and high redox ability [34,45], which was well consistent with H<sub>2</sub>-TPR, O<sub>2</sub>-TPD and EPR analysis.

## 3.2. Catalytic performance of propane oxidation

### 3.2.1. Catalytic activity and stability

The catalytic behaviors of MnO<sub>2</sub>-PS, MnO<sub>2</sub>-R and MnO<sub>2</sub>-B catalysts were evaluated for propane deep catalytic oxidation in the presence of water. The propane conversion as a function of temperature over series catalysts are displayed in Fig. 6A and the *T*<sub>10</sub>, *T*<sub>50</sub> and *T*<sub>90</sub> (the temperature reaching 10%, 50% and 90% propane conversion, respectively) values are summarized in Table 3. As expected, MnO<sub>2</sub>-PS exhibits the best catalytic performance among the series catalysts, followed by MnO<sub>2</sub>-R and MnO<sub>2</sub>-B. The *T*<sub>10</sub>, *T*<sub>50</sub> and *T*<sub>90</sub> values of MnO<sub>2</sub>-PS are 176 °C, 215 °C and 235 °C, which are much lower than those of MnO<sub>2</sub>-R (220 °C, 265 °C and 295 °C) and MnO<sub>2</sub>-B (240 °C, 285 °C and 318 °C), respectively. More specifically, the reaction rate (*r*<sub>C<sub>3</sub>H<sub>8</sub></sub>) and specific activity of series catalyst at 220 °C were calculated to further evaluate the catalytic performance (Table 3). The calculated reaction rate of MnO<sub>2</sub>-PS catalyst is 0.41 μmol·g<sub>cat</sub><sup>−1</sup>·s<sup>−1</sup>, which is 4.6 and 13.6 times higher than those of MnO<sub>2</sub>-R (0.09 μmol·g<sub>cat</sub><sup>−1</sup>·s<sup>−1</sup>) and MnO<sub>2</sub>-B (0.03 μmol·g<sub>cat</sub><sup>−1</sup>·s<sup>−1</sup>), respectively. The specific activity of MnO<sub>2</sub>-PS catalyst is also the highest (0.006 μmol·m<sup>−2</sup>·s<sup>−1</sup>) among the series catalysts. Although the reaction rates are good in agreement with the overall performances of the catalysts, it should be more reasonable to correlate the catalytic activity with the surface active sites (e.g., Mn

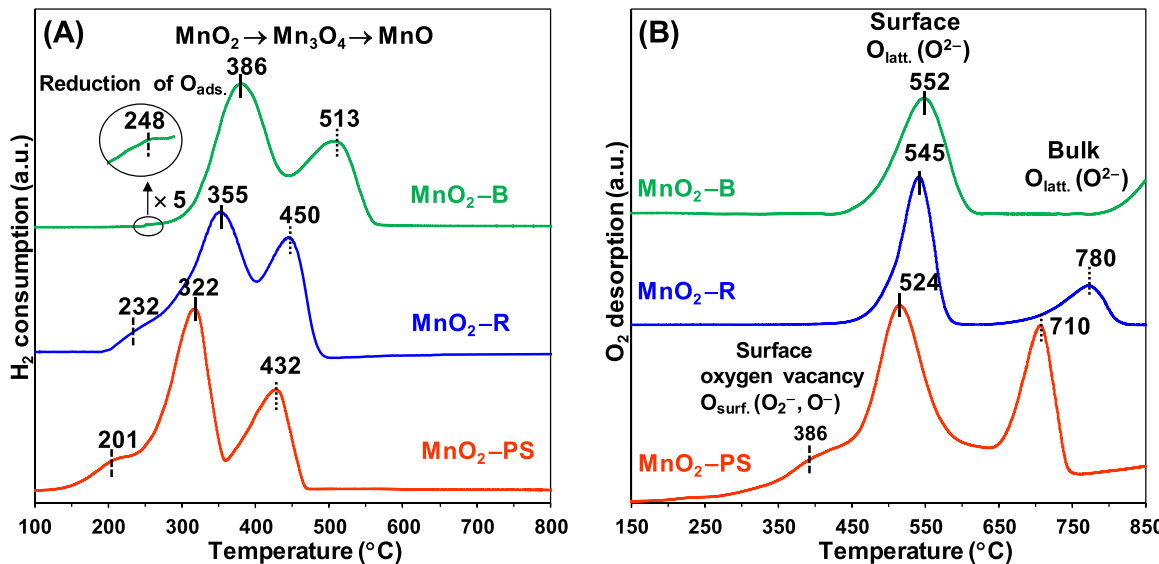


Fig. 3. (A) H<sub>2</sub>-TPR and (B) O<sub>2</sub>-TPD profiles of the MnO<sub>2</sub>-PS, MnO<sub>2</sub>-R and MnO<sub>2</sub>-B catalysts.

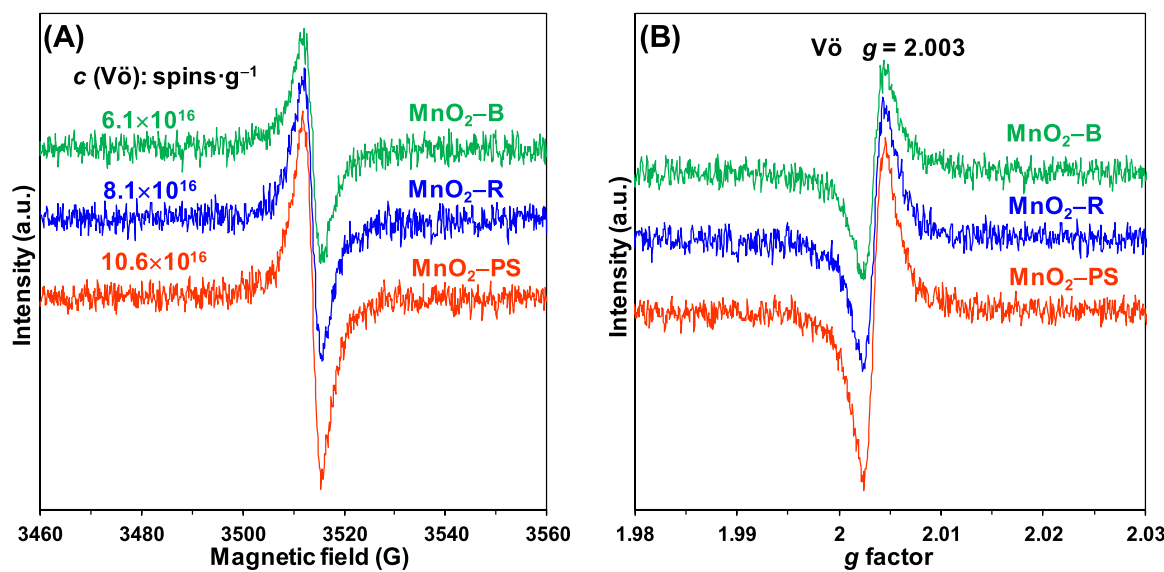


Fig. 4. Low-temperature EPR spectra of (A) magnetic field and (B) g factor for the MnO<sub>2</sub>-PS, MnO<sub>2</sub>-R and MnO<sub>2</sub>-B catalysts.

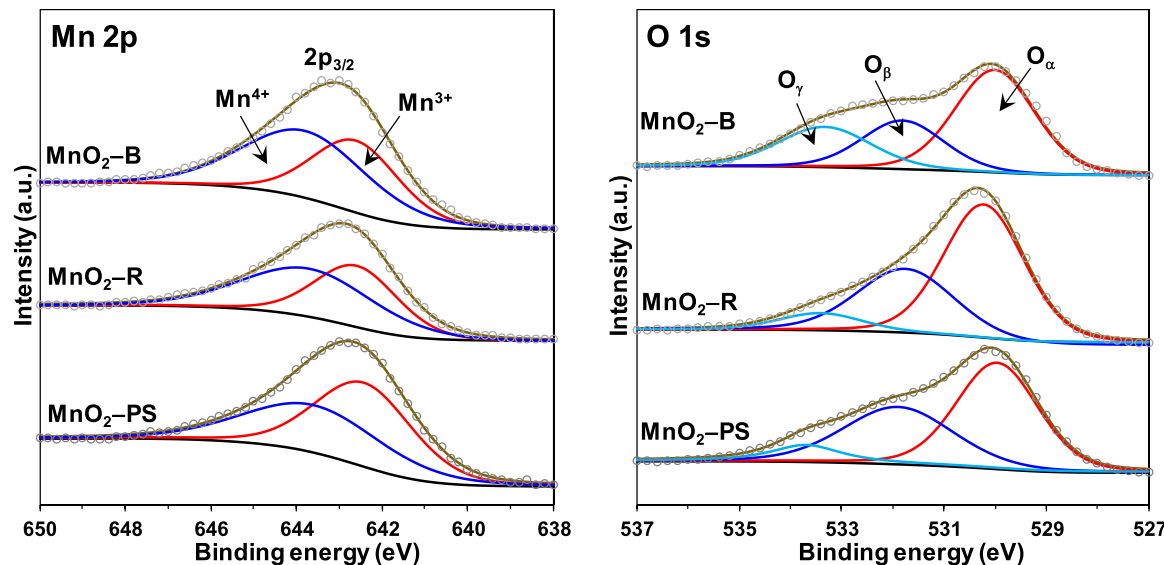


Fig. 5. Deconvoluted XPS spectra of Mn 2p and O 1s core levels for the MnO<sub>2</sub>-PS, MnO<sub>2</sub>-R and MnO<sub>2</sub>-B catalysts.

Table 2

XPS parameters of Mn 2p and O 1 s core levels for the MnO<sub>2</sub>-PS, MnO<sub>2</sub>-R and MnO<sub>2</sub>-B catalysts.

Catalyst	Bonding energy (eV)			AOS <sup>a</sup>	Mn <sup>3+</sup> /Mn <sup>4+</sup> <sup>b</sup>	O <sub>ads</sub> /O <sub>latt</sub> <sup>b</sup>
	Mn <sup>3+</sup>	Mn <sup>4+</sup>	O 1 s (O <sub>α</sub> , O <sub>β</sub> , O <sub>γ</sub> )			
MnO <sub>2</sub> -PS	642.2	643.4	529.9, 531.9, 533.5	3.17	1.22	0.71
MnO <sub>2</sub> -R	642.3	643.5	530.0, 531.8, 533.4	3.38	0.87	0.56
MnO <sub>2</sub> -B	642.3	643.5	529.9, 531.8, 533.4	3.68	0.74	0.48

<sup>a</sup> Average oxidation state (AOS) was calculated by formula: AOS = 8.956–1.126ΔEs, where ΔEs represented the difference of binding energies between two Mn 3s peaks;

<sup>b</sup> Mn<sup>3+</sup>/Mn<sup>4+</sup> and O<sub>ads</sub>/O<sub>latt</sub> were calculated basing on the relative peak area according to Mn 2p and O 1s spectra.

atoms or chemisorbed oxygen species) rather than the catalyst feed amount. Therefore, the iTOFs correlated with the surface Mn atoms and chemisorbed oxygen species of the catalysts were calculated, respectively. As summarized in Tables S2 and S3, whether based on Mn atoms or chemisorbed oxygen species, the MnO<sub>2</sub>-PS catalysts give much higher iTOF value than the MnO<sub>2</sub>-R and MnO<sub>2</sub>-B catalysts, which revealed that better initial catalytic activity of MnO<sub>2</sub>-PS catalysts. In addition, the values of apparent activation energy ( $E_a$ ) were also evaluated in the low propane conversion (0–10%), as shown in Fig. 6B. The MnO<sub>2</sub>-PS catalyst displays a lower  $E_a$  value of 60.6 kJ mol<sup>-1</sup>, followed by MnO<sub>2</sub>-R (76.7 kJ mol<sup>-1</sup>) and MnO<sub>2</sub>-B (79.9 kJ mol<sup>-1</sup>), indicating an easier propane activation ability over MnO<sub>2</sub>-PS, which is well consistent with their catalytic activities. Notably, as shown in Fig. S4, during the propane catalytic oxidation process especially at the low reaction temperatures (<  $T_{50}$ ), the yield of CO<sub>2</sub> over all the three catalysts were slight lower than the conversion of propane, which was more obviously on the MnO<sub>2</sub>-B catalysts. This indicates that in the light-off stage of the catalytic reaction, that is, at low conversion, propane is not completely converted to CO<sub>2</sub>. This because some intermediates may

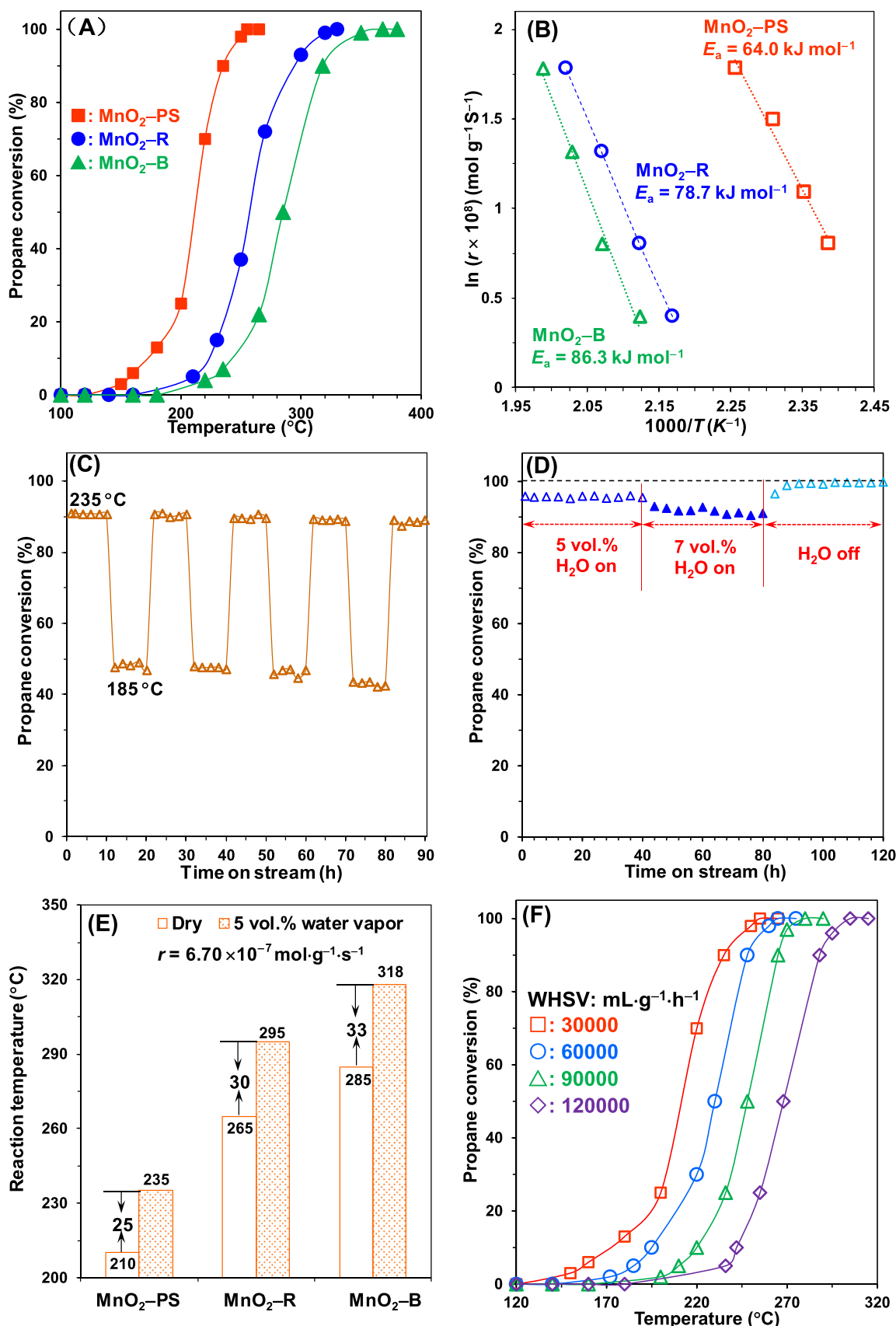


**Fig. 6.** (A) Catalytic activity, (B) Arrhenius plot of different catalysts for propane oxidation, (C) Stability tests of MnO<sub>2</sub>-PS catalyst at 235 and 185 °C, (D) water vapor resistance tests of MnO<sub>2</sub>-PS catalyst at 220 °C, (E) Comparison of reaction temperatures of the MnO<sub>2</sub>-PS, MnO<sub>2</sub>-R and MnO<sub>2</sub>-B catalysts at the reaction rate of  $6.70 \times 10^{-7}$  mol·g<sub>cat</sub><sup>-1</sup>·s<sup>-1</sup> under dry and humid conditions and (F) propane conversion as a function of temperature at different weight hourly space velocities

over MnO<sub>2</sub>-PS catalysts. Reaction conditions: catalyst 100 mg; 5 vol% H<sub>2</sub>O; feed gas 0.2 vol% C<sub>3</sub>H<sub>8</sub>, 2.4 vol% O<sub>2</sub> and balanced by N<sub>2</sub>; WHSV = 30,000 mL·g<sub>cat</sub><sup>-1</sup>·h<sup>-1</sup>.

**Table 3**

Catalytic activities of propane oxidation over the MnO<sub>2</sub>-PS, MnO<sub>2</sub>-R and MnO<sub>2</sub>-B catalysts and reaction rate and specific activity at 220 °C.

Entry	Catalyst	T <sub>10</sub> (°C)	T <sub>50</sub> (°C)	T <sub>90</sub> (°C)	reaction rate (μmol·g <sup>-1</sup> ·s <sup>-1</sup> )	specific activity (μmol·m <sup>-2</sup> ·s <sup>-1</sup> )
1	MnO <sub>2</sub> -PS	176	215	235	0.41	0.006
2	MnO <sub>2</sub> -R	220	260	295	0.09	0.003
3	MnO <sub>2</sub> -B	240	285	318	0.03	0.002

not be further converted at low temperatures, which would be revealed later in *in situ* DRIFTS studies.

To better understand the reactants adsorption behaviors and clarify their relevancy with catalytic reaction rate, a kinetic study over the MnO<sub>2</sub>-PS, MnO<sub>2</sub>-R and MnO<sub>2</sub>-B catalysts were performed. During the kinetics experiments, the reaction rates were obtained when the propane conversion was controlled within 10%, and the kinetic results are summarized in Table S4. The reaction orders of C<sub>3</sub>H<sub>8</sub> and O<sub>2</sub> molecules over MnO<sub>2</sub>-PS, MnO<sub>2</sub>-R and MnO<sub>2</sub>-B catalysts were very close to the first order and zeroth order, respectively, which implied that the oxygen concentration is excessive during the reaction and hardly affects the reaction rate. The result was also similar with the reported propane oxidation and some other VOC oxidation reactions under excess oxygen condition [6,17,46]. However, the high reaction order of C<sub>3</sub>H<sub>8</sub> indicated that the corresponding adsorption concentration on the catalyst surface has a significant influence on the reaction rate. In other words, the better propane adsorption and activation capacity of the catalyst can be one of the important factors to promote the catalytic performance. Among the three catalysts, the MnO<sub>2</sub>-PS catalysts give relative lower reaction order (1.01) than MnO<sub>2</sub>-R (1.14) and MnO<sub>2</sub>-B (1.20) catalysts. It revealed that propane molecules were more inclined to adsorb on the surface of MnO<sub>2</sub>-PS, which probably benefit from its ultra-thin nanosheet and defect-rich porous structure [40,47]. The adsorption energies of propane on surfaces of MnO<sub>2</sub>-PS, MnO<sub>2</sub>-R and MnO<sub>2</sub>-B catalysts would be calculated and discussed later in DFT studies.

The stability of heterogeneous catalysis is extremely important for potential practical applications. The MnO<sub>2</sub>-PS catalyst was employed to evaluate their catalytic stability for propane combustion with time-on-stream. As depicted in Fig. 6C, MnO<sub>2</sub>-PS exhibited excellent stability during the whole durability test period. As displayed in Fig. 6D, it can be seen that almost 95% propane conversion was well maintained at 240 °C for 40 h under a condition in the presence of 5 vol% of H<sub>2</sub>O. Then, increasing the water content from 5 vol% to 7 vol%, while the propane conversion only slightly dropped and nearly unchanged at around 90% for another 40 h. Subsequently, it found that the propane conversion can quickly increase to 100% after cutting off the water addition and still exhibits long-term stability. These results indicate that the limited influence of water on catalytic activity, and the catalytic activity could be almost fully recovered after removing water (Fig. S5), meaning the reversibility of the deactivation. It has been reported that there is competitive adsorption between propane and water molecular on the active sites, thus leading to a decrease in activity [7,34]. Specifically, to get the same reaction rate ( $6.70 \times 10^{-7}$  mol·g<sub>cat</sub><sup>-1</sup>·s<sup>-1</sup>), the reaction temperature of the MnO<sub>2</sub>-PS catalyst under humid conditions (5 vol% H<sub>2</sub>O) needs to increase by 25 °C compared with dry conditions (Fig. 6E), which is lower than for MnO<sub>2</sub>-R (30 °C) and MnO<sub>2</sub>-B (33 °C) catalysts. This indicates that the MnO<sub>2</sub>-PS catalyst has better resistance to water vapor than MnO<sub>2</sub>-R and MnO<sub>2</sub>-B catalysts. In other word, MnO<sub>2</sub>-PS catalyst may has stronger propane adsorption ability than MnO<sub>2</sub>-R and MnO<sub>2</sub>-B catalysts, which would be calculated and discussed later in DFT studies. In addition, the MnO<sub>2</sub>-PS catalyst still had decent performance under higher WHSVs. As shown in Fig. 6F, the WHSV

increased by 4 times from 30,000 to 120,000 mL·g<sub>cat</sub><sup>-1</sup>·h<sup>-1</sup> while the value of T<sub>90</sub> changes from 235 °C to 288 °C, which indicates that the MnO<sub>2</sub>-PS catalyst could meet actual industrial needs even under high WHSV conditions. Furthermore, the used MnO<sub>2</sub>-PS catalyst was characterized by XRD, as shown in Fig. S6, there is hardly noticeable differences in the patterns between the fresh and used catalyst, indicating the excellent structural stability of the MnO<sub>2</sub>-PS catalyst.

### 3.2.2. Comparison with benchmark catalysts

To highlight the excellent catalytic performance of prepared catalysts, the MnO<sub>2</sub>-PS catalyst was compared with that of other typical reported Mn-based catalysts for the propane total oxidation. As summarized in Table 4, the MnO<sub>2</sub>-PS catalyst exhibits much lower T<sub>50</sub> and T<sub>90</sub> values than most those of other Mn-based catalysts under the corresponding reaction conditions, which shows a superior catalytic performance following by the Co<sub>2.3</sub>Mn<sub>0.7</sub>O<sub>4</sub> catalyst. Excitingly, the reaction rate of the MnO<sub>2</sub>-PS catalyst was even much higher than the supported noble catalysts (*i.e.*, Au/α-MnO<sub>2</sub>-100). The above results reveal that the MnO<sub>2</sub>-PS catalyst has advanced catalytic activity, which is a very promising catalyst for the propane abatement in practical application.

## 3.3. Discussion on reaction mechanism of propane oxidation

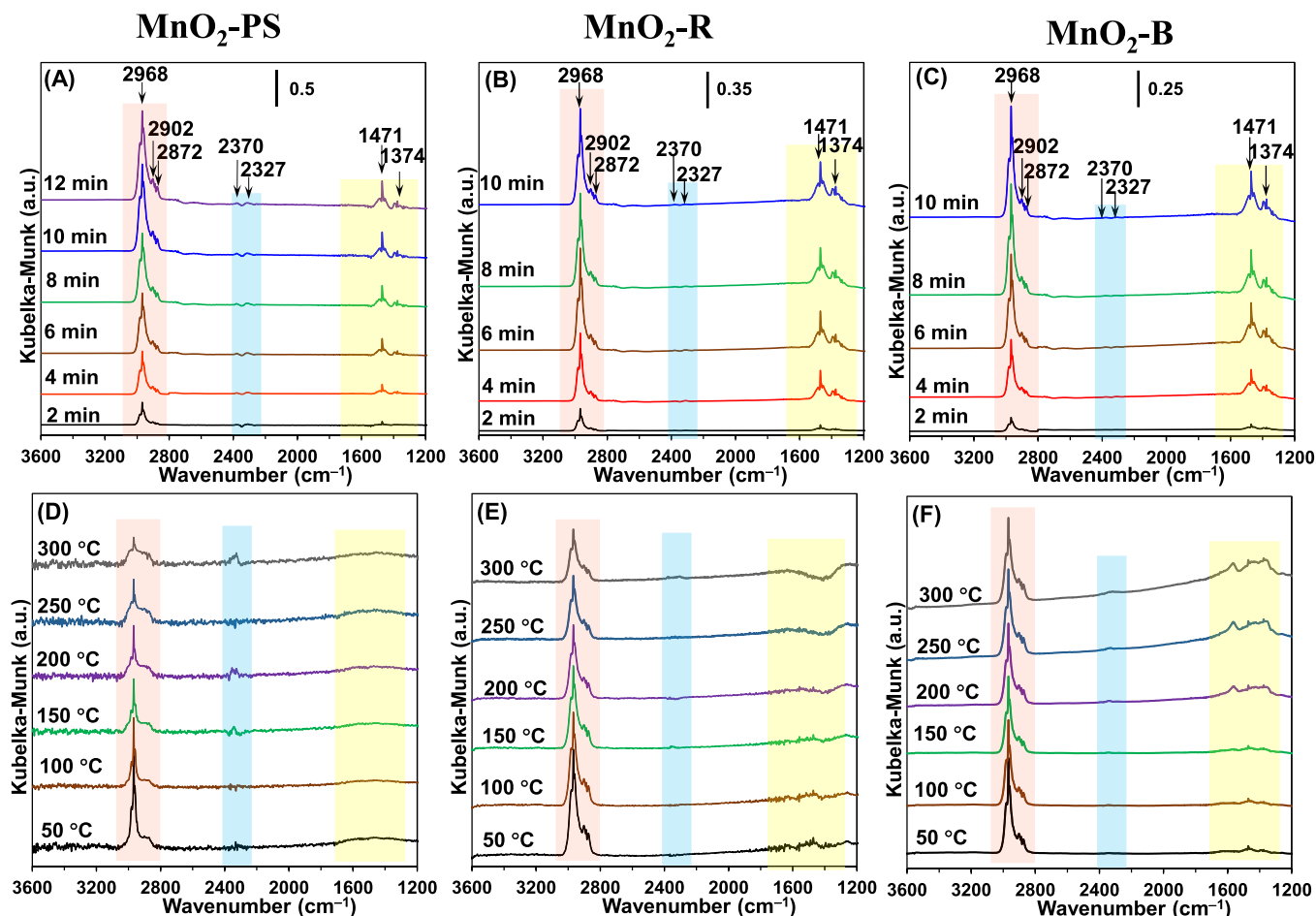
### 3.3.1. Reaction mechanism of propane oxidation

To obtain deeper insight into the reaction mechanism, the time-dependent C<sub>3</sub>H<sub>8</sub> adsorption and oxidation on the fresh MnO<sub>2</sub>-PS, MnO<sub>2</sub>-R and MnO<sub>2</sub>-B catalysts at 200 °C were investigated by *in situ* DRIFTS, and the results are displayed in Fig. 7. The spectra of propane absorption process over series MnO<sub>2</sub> catalysts (catalyst filling amount: 25 mg) was recorded under a flow of 5 vol% C<sub>3</sub>H<sub>8</sub>/N<sub>2</sub> at 200 °C after being pretreated in helium at 300 °C for 1 h (Fig. 7A–C). The bands at 2800–3000 cm<sup>-1</sup> (*ca.* 2968, 2902 and 2872 cm<sup>-1</sup>) are found on all samples, which can be assigned to the C-H stretching vibrations ( $\nu$ ) of gaseous C<sub>3</sub>H<sub>8</sub> and CH<sub>n</sub> (CH<sub>2</sub> or CH<sub>3</sub>) fragments of adsorbed C<sub>3</sub>H<sub>8</sub>, providing the evidences about the cracking of C<sub>3</sub>H<sub>8</sub> [48,50]. Meanwhile, The bands at *ca.* 1471 cm<sup>-1</sup> and 1374 cm<sup>-1</sup> can be attributed to symmetric bending vibrations ( $\delta_s$ ) of CH<sub>2</sub> and asymmetric bending vibrations ( $\delta_{as}$ ) of CH<sub>3</sub>, respectively [5,51]. The signal of these bands gradually intensifies with the exposing time extension of the catalyst in the flow of 5 vol% C<sub>3</sub>H<sub>8</sub>/N<sub>2</sub>. Afterwards, the intensity of bands for all samples was almost unchanged within 10 min, indicating an adsorption equilibrium of C<sub>3</sub>H<sub>8</sub> on the surface of catalysts. It takes 8 min to achieve the propane adsorption equilibrium both for MnO<sub>2</sub>-R (Fig. 7B) and MnO<sub>2</sub>-B (Fig. 7C), but 10 min needed for MnO<sub>2</sub>-PS (Fig. 7A). In addition, to more clearly compare the difference in adsorption ability of propane, the *in-situ* DRIFTS spectra of propane absorption after 15 min on MnO<sub>2</sub>-PS, MnO<sub>2</sub>-R and MnO<sub>2</sub>-B under the same catalyst filling amount were also provided. As shown in Fig. S7, the adsorption intensities of the propane on the MnO<sub>2</sub>-PS catalyst were much higher than MnO<sub>2</sub>-R and MnO<sub>2</sub>-B catalysts, confirming a greater affinity for adsorbing and activating propane on MnO<sub>2</sub>-PS catalyst. Notably, the bands at *ca.* 2370 and 2327 cm<sup>-1</sup> corresponding to asymmetric stretching mode of gas phase CO<sub>2</sub> on MnO<sub>2</sub>-PS catalyst were clearly observed during the whole adsorption process while the signals of CO<sub>2</sub> on MnO<sub>2</sub>-R catalysts were very weak and were even hardly observed on MnO<sub>2</sub>-B catalysts. These phenomena indicated that propane could react with the surface active lattice species on the MnO<sub>2</sub>-PS and MnO<sub>2</sub>-R catalysts to a certain degree even in the absence of external O<sub>2</sub> [17,48,52]. Therefore, compared to MnO<sub>2</sub>-R and MnO<sub>2</sub>-B, the MnO<sub>2</sub>-PS displays the later adsorption equilibrium time with stronger adsorption intensity of propane and the stronger CO<sub>2</sub> signal, implying more reactive

**Table 4**

Comparison of the Mn-based catalysts reported in the literature for propane oxidation and reaction rate at 195 °C.

Catalyst	$C_3H_8$ (ppm)	WHSV ( $mL \cdot g^{-1} \cdot h^{-1}$ )	$T_{50}$ (°C)	$T_{90}$ (°C)	$r_{C_3H_8}$ ( $\mu\text{mol} \cdot \text{g}_{\text{cat}}^{-1} \cdot \text{s}^{-1}$ )	Ref.
M-G-350	8000	12,000	235	265	0.178	[26]
$\alpha$ -MnO <sub>2</sub>	2000	30,000	250	290	0.006	[31]
MnO <sub>x</sub> -BP-13-1	8000	120,000	323	400	0.118	[27]
MnO <sub>2</sub> -SR	2500	12,000 <sup>a</sup>	190	225	0.004	[28]
Mn <sub>0.6</sub> Zr <sub>0.4</sub> O <sub>x</sub>	2000	20,000	280	325	0.013	[40]
MnNi <sub>0.09</sub>	1000	90,000	200	220	0.335	[48]
Co <sub>1</sub> Mn <sub>3</sub> O <sub>x</sub>	2000	18,000	169	207	0.366	[34]
Co <sub>2.3</sub> Mn <sub>0.7</sub> O <sub>4</sub>	3700	117,600	195	225	2.688	[22]
$\alpha$ -MnO <sub>2</sub> -100	2500	12,000 <sup>a</sup>	233	262	0.002	[29]
Au/ $\alpha$ -MnO <sub>2</sub> -100	2500	12,000 <sup>a</sup>	189	216	0.005	[29]
$\alpha$ -MnO <sub>2</sub> -110	2500	30,000	224	262	0.203	[49]
MnO <sub>2</sub> -PS	2000	30,000	214	235	0.149 <sup>b</sup>	This work
MnO <sub>2</sub> -PS	2000	30,000	186	210	0.521	This work
MnO <sub>2</sub> -PS	2000	120,000	225	248	0.367	This work

<sup>a</sup> Gas hourly space velocity (GHSV: h<sup>-1</sup>).<sup>b</sup> with 5 vol% H<sub>2</sub>O.**Fig. 7.** *In-situ* DRIFTS spectra of propane absorption on (A) MnO<sub>2</sub>-PS, (B) MnO<sub>2</sub>-R and (C) MnO<sub>2</sub>-B at 200 °C; *In-situ* DRIFTS spectra of propane oxidation (0.2 vol% C<sub>3</sub>H<sub>8</sub>, 2.4 vol% O<sub>2</sub>/N<sub>2</sub>) on (D) MnO<sub>2</sub>-PS, (E) MnO<sub>2</sub>-R and (F) MnO<sub>2</sub>-B at 50–300 °C.

oxygen species and stronger oxygen mobility with strong propane dissociation ability of propane.

Subsequently, the temperature-dependent *in situ* DRIFT spectra of each MnO<sub>2</sub> sample (catalyst filling amount: 25 mg) were used to detect the intermediates species during propane oxidation and the each spectrum was recorded after 30 min of reaction at the specific temperatures. As shown in Fig. 7D–F, as the reaction temperature increased, the peak intensity of C-H stretching vibrations (2800–3000 cm<sup>-1</sup>) of C<sub>3</sub>H<sub>8</sub> gradually decreased on all catalysts, indicating that propane oxidation

occurred. As the reaction progressed, the peak intensity of the C<sub>3</sub>H<sub>8</sub> decreased the most on the MnO<sub>2</sub>-PS catalyst compared with MnO<sub>2</sub>-R and MnO<sub>2</sub>-B catalysts, accompanied by relative stronger CO<sub>2</sub> peak (2370 and 2327 cm<sup>-1</sup>). Specifically, the peak of CO<sub>2</sub> can be clearly observed even at 50 °C on the MnO<sub>2</sub>-PS catalyst, but only at 150 °C on the MnO<sub>2</sub>-PS catalyst, and at 200 °C on the MnO<sub>2</sub>-B catalyst. In addition, the peak intensity of the intermediates (1200–1800 cm<sup>-1</sup>) on MnO<sub>2</sub>-PS catalyst (Fig. 7D) are much weaker than those on MnO<sub>2</sub>-R (Fig. 7E) and MnO<sub>2</sub>-B catalysts (Fig. 7F). To clarify the intermediates

more clearly, Fig. S8 displayed the enlarged region of the intermediates ( $1200\text{--}1800\text{ cm}^{-1}$ ). Briefly, the peaks at *ca.* 1630 and  $1471\text{ cm}^{-1}$  correspond to the C=C stretching and C-H stretching vibrations of propene, respectively [34]. The multiple peaks at *ca.*  $1560\text{ cm}^{-1}$  ( $\nu_{\text{as}}$  COO<sup>-</sup>),  $1395$  and  $1374\text{ cm}^{-1}$  ( $\delta_{\text{as}}$  CH<sub>3</sub>) and  $1345\text{ cm}^{-1}$  ( $\nu_{\text{s}}$  COO<sup>-</sup>) are mainly related with formate and acetate species [11,53], and the bands corresponding to bidentate carbonate species ( $1315$  and  $1260\text{ cm}^{-1}$ ) are also detected [34,53]. Notably, compared to MnO<sub>2</sub>-PS catalyst, a large amount of intermediates accumulate on the surface of MnO<sub>2</sub>-R and MnO<sub>2</sub>-B catalysts, especially MnO<sub>2</sub>-B catalyst, revealing that a faster decomposition rate of intermediates on MnO<sub>2</sub>-PS than MnO<sub>2</sub>-R and MnO<sub>2</sub>-B. On the basis of above results of *in situ* DRIFTS, the reaction path of the propane oxidation over three MnO<sub>2</sub> catalyst in this work can be proposed *via* following steps: (1) the adsorbed propane is activated and dissociated into CH<sub>n</sub> fragments. 2) the CH<sub>n</sub> fragments species react with the surface active oxygen species to form various intermediates (*i.e.*, propene, carboxylate/carbonate species). 3) gaseous oxygen are adsorbed on the oxygen vacancies and activated to replenish the active oxygen species. 4) the intermediates are rapidly consumed and further completely converted into CO<sub>2</sub> and H<sub>2</sub>O. Although the three MnO<sub>2</sub> catalysts have the same reaction pathway, the different adsorption and activation ability of the propane and O<sub>2</sub> as well as the decomposition ability of the intermediate, which lead to the difference in their catalytic performance. These differences are likely to be closely related to the surface properties of the catalysts, such as oxygen vacancies, reactive oxygen species and redox properties. Base on the above experimental results and discussion, in this work the pathway followed the Mars-van Krevelen mechanism, which was also reported in some other catalyst systems[17,48,54,55].

### 3.3.2. DFT calculation

According to the Mars-van Krevelen mechanism, it can be expected that the propane catalytic oxidation is triggered by its dissociative adsorption on the catalyst surfaces (*i.e.*, the first step of the catalytic cycle), which probably be the important step for the reaction process. Therefore, the adsorption modes of propane on surface of MnO<sub>2</sub>-PS, MnO<sub>2</sub>-R and MnO<sub>2</sub>-B catalysts were studied. The most stable mode of the C<sub>3</sub>H<sub>8</sub> molecule adsorption on the surface of different catalysts and the corresponding adsorption energies shown in Fig. S9. The  $E_{\text{ads}}$  values of C<sub>3</sub>H<sub>8</sub> on the surfaces of MnO<sub>2</sub>-PS, MnO<sub>2</sub>-R and MnO<sub>2</sub>-B catalysts were  $-0.12\text{ eV}$ ,  $0.52\text{ eV}$  and  $1.24\text{ eV}$ , respectively. According to adsorption energy definition, negative adsorption energy suggests that the adsorption process is exothermic and the adsorption system is thermodynamically stable. Contrarily, a positive value corresponds to an endothermic and unstable adsorption. This revealed that C<sub>3</sub>H<sub>8</sub> molecule is easier to adsorb on the surface of the MnO<sub>2</sub>-PS catalysts than MnO<sub>2</sub>-R and MnO<sub>2</sub>-B catalysts. On the other hand, benefiting from the oxygen vacancies, more surface reactive oxygen species were formed over the MnO<sub>2</sub>-PS catalysts that could react with the adsorbed C<sub>3</sub>H<sub>8</sub>. It can be related to the observed CO<sub>2</sub> over MnO<sub>2</sub>-PS catalyst during the *in situ* DRIFTS study of C<sub>3</sub>H<sub>8</sub> adsorption. This result was also well consistent with their catalytic performance, as well as their kinetic studies and water resistance differences.

### 3.3.3. Promotional effects

For transition metal oxides, it was widely accepted that the textural property, the redox behavior and oxygen vacancy were the main factors affecting their catalytic performance for VOCs oxidation [28,30,40,56]. In this work, porous MnO<sub>2</sub> nanosheets (MnO<sub>2</sub>-PS) with abundant oxygen vacancies were successfully prepared by the solvothermal reduction reaction. Compared with MnO<sub>2</sub>-R and MnO<sub>2</sub>-B catalysts, it is inspiring that the MnO<sub>2</sub>-PS catalyst could posses highly efficient activity for catalytic oxidation of C<sub>3</sub>H<sub>8</sub> in the presence of O<sub>2</sub> into CO<sub>2</sub> and H<sub>2</sub>O at low temperature. On the one hand, the relative high specific surface area and internal porosity of the MnO<sub>2</sub>-PS catalysts can provide more active sites that are beneficial to the mass transfer and internal

diffusion, thus facilitates the adsorption of substrate molecules. On the other hand, the redox ability of Mn-based catalyst is mostly governed by the redox cycle between Mn<sup>3+</sup> and Mn<sup>4+</sup> ions, which could be regarded as the driving force during VOCs oxidation [2,21,40]. The higher molar ratio of Mn<sup>3+</sup>/Mn<sup>4+</sup> can correspond to the lower redox potential between Mn<sup>4+</sup> and Mn<sup>3+</sup> cations. In other words, the higher molar ratio of Mn<sup>3+</sup>/Mn<sup>4+</sup>, the stronger redox ability and driving force for oxidation reaction. In this work, MnO<sub>2</sub>-PS catalysts exhibited the best redox ability and highest catalytic activity. As shown in Fig. S10, there is a positive correlation between the propane oxidation rate and the low temperature reducibility. Moreover, the MnO<sub>2</sub>-PS catalysts had more active oxygen species with high mobility and reactivity mainly due to the promotional effects of surface oxygen vacancies. The abundant oxygen vacancies on catalyst can weaken O<sub>2</sub> adsorption energy to adsorb and activate more O<sub>2</sub>, generating more active oxygen species, thus could easily participate in catalytic oxidation reactions and accelerate the catalytic reaction forward [6,7]. To deeply understand the role of oxygen vacancies, the catalytic performance of the MnO<sub>2</sub>-PS catalysts was controlled under continuous alternating N<sub>2</sub> and air (O<sub>2</sub>) atmosphere. Before the test, the catalyst was *in situ* purged at  $200\text{ }^{\circ}\text{C}$  under N<sub>2</sub> flow for 1 h to remove the surface physically and/or chemically adsorbed O<sub>2</sub> and other impurities. As shown in Fig. S11, the catalyst can drive the catalytic oxidation of C<sub>3</sub>H<sub>8</sub> in inert gas, and when the limited active oxygen species are complete consumed the reaction gradually stopped. Interestingly, by switching N<sub>2</sub> to air to the reaction system, because molecular O<sub>2</sub> can be activated on V<sub>O</sub> sites to generate active oxygen species so enables to trigger the catalytic oxidation process again. In fact, the active oxygen species generated at oxygen vacancies (V<sub>O</sub>) are well known to be highly reactive electrophilic radicals and can give rise to the promotion of oxidation reactions. As shown in Fig. 8A, a positive correlation is found between the propane oxidation rate and oxygen vacancy (V<sub>O</sub>) concentration and surface active oxygen species (O<sub>B</sub>). In addition, the propane oxidation rate is also plotted against the surface O<sub>ads</sub>/O<sub>latt</sub> ratio, surface Mn<sup>3+</sup>/Mn<sup>3+</sup> ratio and the specific surface area (Fig. 8B). A good relationship that the catalytic activity of the catalysts correlates well with the oxygen vacancies, redox ability and the specific surface area. Furthermore, the effect of crystal structure and exposed facets cannot be ignored. In fact, it is precisely due to the difference in crystal structure and crystal plane of catalysts that lead to the difference in oxygen vacancies, which are important factors for the difference in catalyst activity [29,57]. We also correlated the iTOF with the surface oxygen vacancies and surface chemisorbed oxygen species (Fig. S12). The more the oxygen vacancies, the more surface oxygen species and the larger the iTOF. From these results, it can concluded that the oxygen vacancies determined by the crystal structure and crystal planes are the most decisive factor of three MnO<sub>2</sub> catalysts in this work that determines the catalytic performance in the propane catalytic oxidation process.

Therefore, as proposed in Scheme 2, the adsorbed and activated C<sub>3</sub>H<sub>8</sub> molecules are oxidized by the active lattice oxygen of MnO<sub>2</sub>-PS accompanied by the reduction of Mn<sup>4+</sup> to Mn<sup>3+</sup> and the formation of oxygen vacancies (V<sub>O</sub>). Concurrently, molecular O<sub>2</sub> was activated on the V<sub>O</sub> accompanied by the re-oxidation of Mn<sup>3+</sup> to Mn<sup>4+</sup> and the replenishment of lattice oxygen. It can be concluded that oxygen vacancies play a critical role in the C<sub>3</sub>H<sub>8</sub> catalytic oxidation process. On the one hand, oxygen vacancies can make the lattice oxygen adjacent to the oxygen vacancy more active [24]. On the other hand, oxygen vacancies not only facilitate the activation of molecular O<sub>2</sub>, but also promote the oxygen mobility from the bulk phase to the surface. Compared with MnO<sub>2</sub>-R and MnO<sub>2</sub>-B, the MnO<sub>2</sub>-PS with porous nanosheet and rough surface shows a high surface area that is beneficial to the exposure of more active sites and the mass transfer. Moreover, the MnO<sub>2</sub>-PS catalyst affords easier propane adsorption ability, abundant oxygen vacancies, stronger reducibility and higher oxygen mobility, which are the key factors for its excellent catalytic performance.

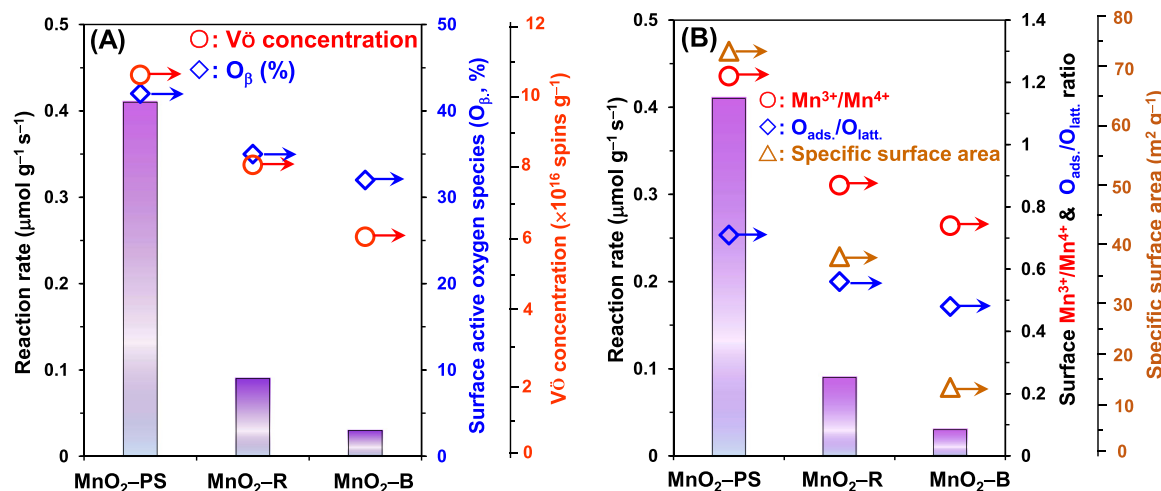
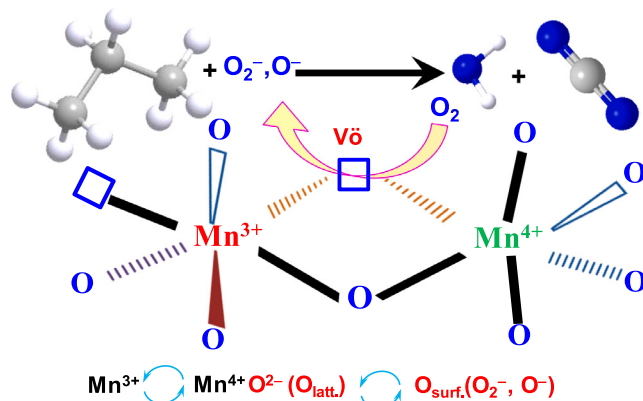


**Fig. 8.** The relationship between reaction rate and (A) oxygen vacancy ( $\text{V}\ddot{\text{o}}$ ) concentration and surface active oxygen species ( $\text{O}_\beta$ ); (B) surface species concentration and specific surface area. Reaction conditions: 220 °C; catalyst 100 mg; 5 vol%  $\text{H}_2\text{O}$ , feed gas 0.2 vol%  $\text{C}_3\text{H}_8$ , 2.4 vol%  $\text{O}_2$  and balanced by  $\text{N}_2$ ; WHSV = 30,000  $\text{mL}\cdot\text{g}_{\text{cat}}^{-1}\cdot\text{h}^{-1}$ .



**Scheme 2.** The plausible reaction mechanism of propane oxidative over the  $\text{MnO}_2\text{-PS}$  catalyst.

#### 4. Conclusions

In summary, a novel porous  $\text{MnO}_2$  nanosheet with abundant oxygen vacancies ( $\text{MnO}_2\text{-PS}$ ) was prepared as highly active and stable catalyst for catalytic oxidation of propane at low temperature. The reaction rate of  $\text{MnO}_2\text{-PS}$  was almost 4.6 and 13.6 times higher than those of  $\text{MnO}_2\text{-R}$  and  $\text{MnO}_2\text{-B}$  catalysts, respectively. The H<sub>2</sub>-TPR, O<sub>2</sub>-TPD, XPS, EPR and DFT results provided evidences of rich oxygen vacancies, more active oxygen species, strong redox properties, fast surface oxygen mobility and easier propane adsorption ability on the  $\text{MnO}_2\text{-PS}$  catalysts, which are positively responsible for its outstanding performance. *In situ* DRIFTS analysis demonstrated that the propane catalytic oxidation on  $\text{MnO}_2\text{-PS}$  catalysts is dominated by the Mars-van Krevelen mechanism. It was demonstrated that more Vö can activate and transform more molecular  $\text{O}_2$  into more highly reactive oxygen species, thus can accelerate the cleavage of C-H bond of adsorbed propane on the catalyst and the dissociation of intermediates in the actual catalytic oxidation process. This work may provide a facile and reliable strategy for designing high-activity catalysts for the degradation of VOCs in practical environmental applications.

#### CRedit authorship contribution statement

**Shipeng Wu:** Investigation, Methodology, Formal analysis, Writing

– original draft. **Huimin Liu:** Methodology, Formal analysis. **Zhen Huang:** Formal analysis, Funding acquisition, Writing - review & revision. **Hualong Xu:** Resources, Supervision, Funding acquisition. **Wei Shen:** Resources, Conceptualization, Supervision, Writing - review & revision, Funding acquisition.

#### Declaration of Competing Interest

All authors declare that there are no conflicts of interest, financial or otherwise in this work. And there are no other relationships or activities that can appear to have influenced the submitted work.

#### Acknowledgements

This work was supported by the Shanghai Science and Technology Committee (No. 14DZ2273900) and also funded by Shaanxi Yanchang Petroleum (Group) Co. Ltd.

#### Appendix A. Supporting information

Supplementary data associated with this article can be found in the online version at doi:10.1016/j.apcatb.2022.121387.

#### References

- [1] Y. Guo, M. Wen, G. Li, T. An, Recent advances in VOC elimination by catalytic oxidation technology onto various nanoparticles catalysts: a critical review, *Appl. Catal. B Environ.* 281 (2021) 119447–119466.
- [2] C. He, J. Cheng, X. Zhang, M. Douthwaite, S. Pattisson, Z. Hao, Recent advances in the catalytic oxidation of volatile organic compounds: a review based on pollutant sorts and sources, *Chem. Rev.* 119 (2019) 4471–4568.
- [3] C. Feng, Q. Gao, G. Xiong, Y. Chen, Y. Pan, Z. Fei, Y. Li, Y. Lu, C. Liu, Y. Liu, Defect engineering technique for the fabrication of  $\text{LaCoO}_3$  perovskite catalyst via urea treatment for total oxidation of propane, *Appl. Catal. B Environ.* 304 (2022) 121005–121016.
- [4] Y. Guo, M. Wen, S. Song, Q. Liu, G. Li, T. An, Enhanced catalytic elimination of typical VOCs over  $\text{ZnCoOx}$  catalyst derived from *in situ* pyrolysis of  $\text{ZnCo}$  bimetallic zeolitic imidazolate frameworks, *Appl. Catal. B Environ.* 308 (2022) 121212–121221.
- [5] Z. Wang, Z. Huang, J.T. Brosnan, S. Zhang, Y. Guo, Y. Guo, L. Wang, Y. Wang, W. Zhan, Ru/ $\text{CeO}_2$  catalyst with optimized  $\text{CeO}_2$  Support morphology and surface facets for propane combustion, *Environ. Sci. Technol.* 53 (2019) 5349–5358.
- [6] K. Zha, W. Sun, Z. Huang, H. Xu, W. Shen, Insights into high-performance monolith catalysts of  $\text{Co}_3\text{O}_4$  nanowires grown on nickel foam with abundant oxygen vacancies for formaldehyde oxidation, *ACS Catal.* 10 (2020) 12127–12138.
- [7] G. Chai, W. Zhang, L.F. Liotta, M. Li, Y. Guo, A. Giroir-Fendler, Total oxidation of propane over  $\text{Co}_3\text{O}_4$ -based catalysts: Elucidating the influence of Zr dopant, *Appl. Catal. B Environ.* 298 (2021) 120606–120620.

- [8] W. Liu, S. Yang, Q. Zhang, T. He, Y. Luo, J. Tao, D. Wu, H. Peng, Insights into flower-like Al2O3 spheres with rich unsaturated pentacoordinate Al3+ sites stabilizing Ru-CeO<sub>x</sub> for propane total oxidation, *Appl. Catal. B Environ.* 292 (2021) 120171–120183.
- [9] L. Yang, Q. Liu, R. Han, K. Fu, Y. Su, Y. Zheng, X. Wu, C. Song, N. Ji, X. Lu, D. Ma, Confinement and synergy effect of bimetallic Pt-Mn nanoparticles encapsulated in ZSM-5 zeolite with superior performance for acetone catalytic oxidation, *Appl. Catal. B Environ.* 309 (2022) 121224–121237.
- [10] Z. Hu, X. Liu, D. Meng, Y. Guo, Y. Guo, G. Lu, Effect of ceria crystal plane on the physicochemical and catalytic properties of Pd/Ceria for CO and propane oxidation, *ACS Catal.* 6 (2016) 2265–2279.
- [11] P.-P. Zhao, J. Chen, H.-B. Yu, B.-H. Cen, W.-Y. Wang, M.-F. Luo, J.-Q. Lu, Insights into propane combustion over MoO<sub>3</sub> promoted Pt/ZrO<sub>2</sub> catalysts: The generation of Pt-MoO<sub>3</sub> interface and its promotional role on catalytic activity, *J. Catal.* 391 (2020) 80–90.
- [12] E.V. Kovalyov, E.M. Sadovskaya, B.S. Bal'zhinimaev, Kinetic features of the deep oxidation of propane over a Pt/fiberglass catalyst, *Chem. Eng. J.* 349 (2018) 547–553.
- [13] W.-M. Liao, X.-X. Fang, B.-H. Cen, J. Chen, Y.-R. Liu, M.-F. Luo, J.-Q. Lu, Deep oxidation of propane over WO<sub>3</sub>-promoted Pt/BN catalysts: the critical role of Pt-WO<sub>3</sub> interface, *Appl. Catal. B: Environ.* 272 (2020) 118858–118868.
- [14] Q. Wu, J. Yan, M. Jiang, Q. Dai, J. Wu, M.N. Ha, Q. Ke, X. Wang, W. Zhan, Phosphate-assisted synthesis of ultrathin and thermally stable alumina nanosheets as robust Pd support for catalytic combustion of propane, *Appl. Catal. B Environ.* 286 (2021) 119949–119961.
- [15] W. Zhang, K. Lassen, C. Desorme, J.L. Valverde, A. Giroir-Fendler, Effect of the precipitation pH on the characteristics and performance of Co<sub>3</sub>O<sub>4</sub> catalysts in the total oxidation of toluene and propane, *Appl. Catal. B Environ.* 282 (2021) 119566–119576.
- [16] X. Zhang, R. You, D. Li, T. Cao, W. Huang, Reaction sensitivity of ceria morphology effect on Ni/CeO<sub>2</sub> catalysis in propane oxidation reactions, *ACS Appl. Mater. Interfaces* 9 (2017) 35897–35907.
- [17] K. Zha, H. Liu, L. Xue, Z. Huang, H. Xu, W. Shen, Co<sub>3</sub>O<sub>4</sub> nanoparticle-decorated SiO<sub>2</sub> nanotube catalysts for propane oxidation, *ACS Appl. Nano Mater.* 4 (2021) 8937–8949.
- [18] G. Li, K. He, F. Zhang, G. Jiang, Z. Zhao, Z. Zhang, J. Cheng, Z. Hao, Defect enhanced CoMnNiO<sub>x</sub> catalysts derived from spent ternary lithium-ion batteries for low-temperature propane oxidation, *Appl. Catal. B Environ.* 309 (2022) 121231–121244.
- [19] S. Wu, H. Zhang, Q. Cao, Q. Zhao, W. Fang, Efficient imine synthesis via oxidative coupling of alcohols with amines in an air atmosphere using a mesoporous manganese-zirconium solid solution catalyst, *Catal. Sci. Technol.* 11 (2021) 810–822.
- [20] S.C. Kim, W.G. Shim, Catalytic combustion of VOCs over a series of manganese oxide catalysts, *Appl. Catal. B Environ.* 98 (2010) 180–185.
- [21] P. Wu, X. Jin, Y. Qiu, D. Ye, Recent progress of thermocatalytic and photo/thermocatalytic oxidation for VOCs purification over manganese-based oxide catalysts, *Environ. Sci. Technol.* 55 (2021) 4268–4286.
- [22] B. Faure, P. Alphonse, Co-Mn-Oxide spinel catalysts for CO and propane oxidation at mild temperature, *Appl. Catal. B Environ.* 180 (2016) 715–725.
- [23] Y. Wang, S. Aghamohammadi, D. Li, K. Li, R. Farrauto, Structure dependence of Nb<sub>2</sub>O<sub>5</sub>-X supported manganese oxide for catalytic oxidation of propane: enhanced oxidation activity for MnO<sub>x</sub> on a low surface area Nb<sub>2</sub>O<sub>5</sub>-X, *Appl. Catal. B Environ.* 244 (2019) 438–447.
- [24] N. Huang, Z. Qu, C. Dong, Y. Qin, X. Duan, Superior performance of  $\alpha$ - $\beta$ -MnO<sub>2</sub> for the toluene oxidation: active interface and oxygen vacancy, *Appl. Catal. A Gen.* 560 (2018) 195–205.
- [25] Y. Wang, J. Wu, G. Wang, D. Yang, T. Ishihara, L. Guo, Oxygen vacancy engineering in Fe doped akhtenskite-type MnO<sub>2</sub> for low-temperature toluene oxidation, *Appl. Catal. B Environ.* 285 (2021) 119873–119889.
- [26] B. Puertolas, A. Smith, I. Vázquez, A. Dejoz, A. Moragues, T. Garcia, B. Solsona, The different catalytic behaviour in the propane total oxidation of cobalt and manganese oxides prepared by a wet combustion procedure, *Chem. Eng. J.* 229 (2013) 547–558.
- [27] D. Lin, X. Feng, C. Cao, H. Xue, Y. Luo, Q. Qian, L. Zeng, B. Huang, S. Yang, Q. Chen, Novel bamboo-mediated biosynthesis of MnO<sub>x</sub> for efficient low-temperature propane oxidation, *ACS Sustain. Chem. Eng.* 8 (2020) 11446–11455.
- [28] Y. Jian, X. Feng, M. Tian, Z. Jiang, C. He, Birnessite-type short rod-like MnO<sub>2</sub> achieving propane low-temperature destruction: benign synthesis strategy and reaction mechanism determination, *Appl. Surf. Sci.* 559 (2021) 149905–149916.
- [29] Y. Jian, Z. Jiang, C. He, M. Tian, W. Song, G. Gao, S. Chai, Crystal facet engineering induced robust and sinter-resistant Au/ $\alpha$ -MnO<sub>2</sub> catalyst for efficient oxidation of propane: indispensable role of oxygen vacancies and Au<sup>δ+</sup> species, *Catal. Sci. Technol.* 11 (2021) 1089–1097.
- [30] F. Shi, F. Wang, H. Dai, J. Dai, J. Deng, Y. Liu, G. Bai, K. Ji, C.T. Au, Rod-, flower-, and dumbbell-like MnO<sub>2</sub>: Highly active catalysts for the combustion of toluene, *Appl. Catal. A Gen.* 433–434 (2012) 206–213.
- [31] Y. Xie, Y. Yu, X. Gong, Y. Guo, Y. Guo, Y. Wang, G. Lu, Effect of the crystal plane figure on the catalytic performance of MnO<sub>2</sub> for the total oxidation of propane, *CrystEngComm* 17 (2015) 3005–3014.
- [32] H. Sun, X. Yu, X. Yang, X. Ma, M. Lin, C. Shao, Y. Zhao, F. Wang, M. Ge, Au/Rod-like MnO<sub>2</sub> catalyst via thermal decomposition of manganite precursor for the catalytic oxidation of toluene, *Catal. Today* 332 (2019) 153–159.
- [33] S. Wu, Y. Wang, Q. Cao, Q. Zhao, W. Fang, Efficient imine formation by oxidative coupling at low temperature catalyzed by high-surface-area mesoporous CeO<sub>2</sub> with exceptional redox property, *Chem. Eur. J.* 27 (2021) 3019–3028.
- [34] G. Li, N. Li, Y. Sun, Y. Qu, Z. Jiang, Z. Zhao, Z. Zhang, J. Cheng, Z. Hao, Efficient defect engineering in Co-Mn binary oxides for low-temperature propane oxidation, *Appl. Catal. B Environ.* 282 (2021) 119512–119522.
- [35] Y. Liu, N. Ran, R. Ge, J. Liu, W. Li, Y. Chen, L. Feng, R. Che, Porous Mn-doped cobalt phosphide nanosheets as highly active electrocatalysts for oxygen evolution reaction, *Chem. Eng. J.* 425 (2021) 131642–131653.
- [36] Y. Yang, X. Su, L. Zhang, P. Kerns, L. Achola, V. Hayes, R. Guardokus, S.L. Suib, J. He, Intercalating MnO<sub>2</sub> nanosheets with transition metal cations to enhance oxygen evolution, *ChemCatChem* 11 (2019) 1689–1700.
- [37] T. Gao, J. Chen, W. Fang, Q. Cao, W. Su, F. Dumégnil, Ru/Mn<sub>x</sub>Ce<sub>1</sub>O<sub>y</sub> catalysts with enhanced oxygen mobility and strong metal-support interaction: exceptional performances in 5-hydroxymethylfurfural base-free aerobic oxidation, *J. Catal.* 368 (2018) 53–68.
- [38] S. Rong, P. Zhang, F. Liu, Y. Yang, Engineering crystal facet of  $\alpha$ -MnO<sub>2</sub> nanowire for highly efficient catalytic oxidation of carcinogenic airborne formaldehyde, *ACS Catal.* 8 (2018) 3435–3446.
- [39] T. Gao, Y. Yin, G. Zhu, Q. Cao, W. Fang, Co<sub>3</sub>O<sub>4</sub> NPs decorated Mn-Co-O solid solution as highly selective catalyst for aerobic base-free oxidation of 5-HMF to 2,5-FDCA in water, *Catal. Today* 355 (2020) 252–262.
- [40] K. Zeng, X. Li, C. Wang, Z. Wang, P. Guo, J. Yu, C. Zhang, X.S. Zhao, Three-dimensionally macroporous MnZrO<sub>x</sub> catalysts for propane combustion: Synergistic structure and doping effects on physicochemical and catalytic properties, *J. Colloid Interface Sci.* 572 (2020) 281–296.
- [41] H. Zhang, T. Gao, Q. Cao, W. Fang, Tailoring the reactive oxygen species in mesoporous NiO for selectivity-controlled aerobic oxidation of 5-hydroxymethylfurfural on a loaded Pt catalyst, *ACS Sustain. Chem. Eng.* 9 (2021) 6056–6067.
- [42] M. Piumetti, D. Fino, N. Russo, Mesoporous manganese oxides prepared by solution combustion synthesis as catalysts for the total oxidation of VOCs, *Appl. Catal. B Environ.* 163 (2015) 277–287.
- [43] X. Zhang, H. Zhao, Z. Song, W. Liu, J. Zhao, Za Ma, M. Zhao, Y. Xing, Insight into the effect of oxygen species and Mn chemical valence over MnO<sub>x</sub> on the catalytic oxidation of toluene, *Appl. Surf. Sci.* 493 (2019) 9–17.
- [44] T. Xue, R. Li, Y. Gao, Q. Wang, Iron mesh-supported vertically aligned Co-Fe layered double oxide as a novel monolithic catalyst for catalytic oxidation of toluene, *Chem. Eng. J.* 384 (2020) 123284–123295.
- [45] S. Mo, Q. Zhang, J. Li, Y. Sun, Q. Ren, S. Zou, Q. Zhang, J. Lu, M. Fu, D. Mo, J. Wu, H. Huang, D. Ye, Highly efficient mesoporous MnO<sub>2</sub> catalysts for the total toluene oxidation: Oxygen-Vacancy defect engineering and involved intermediates using in situ DRIFTS, *Appl. Catal. B Environ.* 264 (2020) 118464–118480.
- [46] S. Xie, Y. Liu, J. Deng, J. Yang, X. Zhao, Z. Han, K. Zhang, H. Dai, Insights into the active sites of ordered mesoporous cobalt oxide catalysts for the total oxidation of o-xylene, *J. Catal.* 352 (2017) 282–292.
- [47] Y.-R. Liu, X. Li, W.-M. Liao, A.-P. Jia, Y.-J. Wang, M.-F. Luo, J.-Q. Lu, Highly active Pt/BN catalysts for propane combustion: the roles of support and reactant-induced evolution of active sites, *ACS Catal.* 9 (2019) 1472–1481.
- [48] L. Chen, J. Jia, R. Ran, X. Song, Nickel doping MnO<sub>2</sub> with abundant surface pits as highly efficient catalysts for propane deep oxidation, *Chem. Eng. J.* 369 (2019) 1129–1137.
- [49] C. Feng, G. Xiong, Y. Li, Q. Gao, Y. Pan, Z. Fei, Y. Li, Y. Lu, C. Liu, Y. Liu, High-precision synthesis of  $\alpha$ -MnO<sub>2</sub> nanowires with controllable crystal facets for propane oxidation, *CrystEngComm* 23 (2021) 7602–7614.
- [50] Y. Luo, Y. Zheng, X. Feng, D. Lin, Q. Qian, X. Wang, Y. Zhang, Q. Chen, X. Zhang, Controllable P doping of the LaCoO<sub>3</sub> catalyst for efficient propane oxidation: optimized surface co distribution and enhanced oxygen vacancies, *ACS Appl. Mater. Interfaces* 12 (2020) 23789–23799.
- [51] Z. Hu, Z. Wang, Y. Guo, L. Wang, Y. Guo, J. Zhang, W. Zhan, Total oxidation of propane over a Ru/CeO<sub>2</sub> catalyst at low temperature, *Environ. Sci. Technol.* 52 (2018) 9531–9541.
- [52] Y. Zheng, Y. Chen, E. Wu, X. Liu, B. Huang, H. Xue, C. Cao, Y. Luo, Q. Qian, Q. Chen, Amorphous boron dispersed in LaCoO<sub>3</sub> with large oxygen vacancies for efficient catalytic propane oxidation, *Chem. Eur. J.* 27 (2021) 4738–4745.
- [53] W. Zhu, X. Chen, C. Li, Z. Liu, C. Liang, Manipulating morphology and surface engineering of spinel cobalt oxides to attain high catalytic performance for propane oxidation, *J. Catal.* 396 (2021) 179–191.
- [54] H. Huang, Y. Xu, Q. Feng, D.Y.C. Leung, Low temperature catalytic oxidation of volatile organic compounds: a review, *Catal. Sci. Technol.* 5 (2015) 2649–2669.
- [55] V.V. Kaichev, D. Teschner, A.A. Sarava, S.S. Kosolobov, A.Y. Gladky, I.P. Prosvirin, N.A. Rudina, A.B. Ayupov, R. Blume, M. Hävecker, A. Knop-Gericke, R. Schlögl, A. V. Latyshev, V.I. Buktiyarov, Evolution of self-sustained kinetic oscillations in the catalytic oxidation of propane over a nickel foil, *J. Catal.* 334 (2016) 23–33.
- [56] W. Hua, C. Zhang, Y. Guo, G. Chai, C. Wang, Y. Guo, L. Wang, Y. Wang, W. Zhan, An efficient Sn<sub>y</sub>Mn<sub>1-y</sub>O<sub>x</sub> composite oxide catalyst for catalytic combustion of vinyl chloride emissions, *Appl. Catal. B Environ.* 255 (2019) 117748–117757.
- [57] Y. Jian, M. Tian, C. He, J. Xiong, Z. Jiang, H. Jin, L. Zheng, R. Albilali, J.-W. Shi, Efficient propane low-temperature destruction by Co<sub>3</sub>O<sub>4</sub> crystal facets engineering: unveiling the decisive role of lattice and oxygen defects and surface acid-base pairs, *Appl. Catal. B Environ.* 283 (2021) 119657–119670.